Global Ozone Monitoring Experiment-2 (GOME-2) Daily and Monthly Level 3 Products of Atmospheric Trace Gas Columns

Ka Lok Chan[1,2], Pieter Valks[2], Klaus-Peter Heue[2,3], Ronny Lutz[2], Pascal Hedelt[2], Diego Loyola[2], Gaia Pinardi[4], Michel Van Roozendael[4], François Hendrick[4], Thomas Wagner[5], Vinod Kumar[5], Alkis Bais[6], Ankie Piters[7], Hitoshi Irie[8], Hisahiro Takashima[9,10], Yugo Kanaya[10], Yongjoo Choi[11], Kihong Park[12], Jihyo Chong[12,13], Alexander Cede[14], Udo Frieß[15], Andreas Richter[16], Jianzhong Ma[17], Nuria Benavent[18], Robert Holla[19], Oleg Postylyakov[20], Claudia Rivera Cárdenas[21], and Mark Wenig[22]

[1]Rutherford Appleton Laboratory Space, Harwell Oxford, United Kingdom
[2]Remote Sensing Technology Institute, German Aerospace Center (DLR), Oberpfaffenhofen, Germany
[3]Department of Aerospace and Geodesy, Technical University of Munich (TUM), Munich, Germany
[4]Royal Belgian Institute for Space Aeronomy (BIRA-IASB), Brussels, Belgium
[5]Max Planck Institute for Chemistry (MPIC), Mainz, Germany
[6]Laboratory of Atmospheric Physics, Aristotle University of Thessaloniki (AUTH), Thessaloniki, Greece
[7]Royal Netherlands Meteorological Institute (KNMI), De Bilt, Netherlands
[8]Center for Environmental Remote Sensing (CEReS), Chiba University, Chiba, Japan
[9]Faculty of Science, Fukuoka University, Fukuoka , Japan
[10]Research Institute for Global Change (RIGC), Japan Agency for Marine-Earth Science and Technology (JAMSTEC), Yokohama, Japan
[11]Department of Environmental Science, Hankuk University of Foreign Studies, Seoul, Korea
[12]School of Earth Sciences and Environmental Engineering, Gwangju Institute of Science and Technology, Gwangju, Korea
[13]Environmental Management Division, Yeongsan River Basin Environmental Office, Gwangju, Korea
[14]LuftBlick, Kreith, Austria
[15]Institute of Environmental Physics, University of Heidelberg, Heidelberg, Germany
[16]Institute of Environmental Physics, University of Bremen, Bremen, Germany
[17]Chinese Academy of Meteorology Science, China Meteorological Administration, Beijing, China
[18]Department of Atmospheric Chemistry and Climate, Institute of Physical Chemistry Rocasolano (CSIC), Madrid, Spain
[19]Deutscher Wetterdienst (DWD), Hohenpeißenberg, Germany
[20]A.M. Obukhov Institute of Atmospheric Physics (IAP), Russian Academy of Sciences (RAS), Moscow, Russia
[21]Instituto de Ciencias de la Atmósfera y Cambio Climático, Universidad Nacional Autónoma de México, Mexico City, Mexico
[22]Meteorological Institute (MIM), Ludwig-Maximilians-Universität München (LMU), Munich, Germany

Correspondence: Ka Lok Chan (ka.chan@stfc.ac.uk)

Abstract.

We introduce the new GOME-2 daily and monthly level 3 product of total column ozone (O_3), total and tropospheric column nitrogen dioxide (NO_2), total column water vapour, total column bromine oxide (BrO), total column formaldehyde (HCHO) and total column sulphur dioxide (SO_2). The GOME-2 level 3 products are aimed to provide easily translatable and user-friendly data sets to the scientific community for scientific progress as well as satisfying public interest. The purpose of this paper is to present the theoretical basis as well as the verification and validation of the GOME-2 daily and monthly level 3 products.

The GOME-2 level 3 products are produced using the overlapping area weighting method. Details of the gridding algorithm are presented. The spatial resolution of the GOME-2 level 3 products is selected based on sensitivity study. The consistency of the resulting level 3 products among three GOME-2 sensors is investigated through time series of global averages, zonal averages, and bias. The accuracy of the products is validated by comparing to ground-based observations. The verification and validation results show that the GOME-2 level 3 products are consistent with the level 2 data. Small discrepancies are found among three GOME-2 sensors, which are mainly caused by the differences in instrument characteristic and level 2 processor. The comparison of GOME-2 level 3 products to ground-based observations in general shows very good agreement, indicating the products are consistent and fulfil the requirements to serve the scientific community and general public.

1   Introduction

Satellite remote sensing observations provide indispensable spatio-temporal information of atmospheric composition on a global scale. Various atmospheric trace gases can be retrieved from nadir viewing satellite spectroscopic observations in the ultraviolet (UV) and visible (Vis) spectral range. This type of observation has long been conducted since the Global Ozone Monitoring Experience (GOME) mission launched in 1995 (Burrows et al., 1999). Together with other follow up satellite borne spectrometers, for example, SCanning Imaging Absorption SpectroMeter for Atmospheric CHartographY (SCIAMACHY; Bovensmann et al. (1999)), Global Ozone Monitoring Experience 2 (GOME-2; Callies et al. (2000)) and Ozone Monitoring Instrument (OMI; Levelt et al. (2006)), TROPOspheric Monitoring Instrument (TROPOMI; Veefkind et al. (2012)), these observations provide a global record of earthshine radiance in the UV, VIS and NIR (UVN) spectral range for more than 25 years. The processing of satellite observation of trace gas column involves two major steps, (1) conversion of raw spectral channel counts (level 0 data) to geolocation and radiometric calibrated radiance and irradiance data (level 1B data), and (2) the retrieval of trace gas columns (level 2 data) from level 1B data which includes spectral retrieval of trace gas slant columns and subsequently convert them to vertical columns. To ensure the accuracy and consistency of satellite observations, GOME-2 data are processed in stable operational environments within the framework of Satellite Application Facility on Atmospheric Composition Monitoring (AC SAF). The level 0 to level 1B conversion is processed by European Organisation for the Exploitation of Meteorological Satellites (EUMETSAT), while the level 1B to level 2 is processed by German Aerospace Center (DLR).

The GOME-2 level 2 data are orbital-swath scientific products. A level 2 data file contains observations within a single orbit. Trace gas columns are expressed in the satellite viewing geometry of reference using across-track and along-track position. In addition, the satellite measurement footprint is not in regular latitude-longitude grid and often multiple pixels overlapping at the edges of orbit within a day. Using this kind of scientific product requires very good knowledge of the satellite product, especially when averaging multiple measurements to generate daily or monthly maps. In order to provide a user-friendly satellite product, we have projected the GOME-2 level 2 data onto a regular latitude-longitude grid to generate operational level 3 products. The purpose of this document is to present the theoretical basis, verification and validation of the GOME-2 level 3 daily and monthly gridded products. These products include global daily and monthly mean of total column ozone (O_3), total and tropospheric column nitrogen dioxide (NO_2), total column bromine oxide (BrO), total column water vapour

(H_2O), total column formaldehyde (HCHO), and total column sulphur dioxide (SO_2). Compared to satellite observations from OMI and TROPOMI which are measuring at noon/early afternoon, GOME-2 measurements in the morning provide addition information on the temporal/diurnal variation of these atmospheric trace gases.

The paper is organized as follows. Section 2.1 describes the GOME-2 instruments. A brief description of each GOME-2 level 2 trace gas product can be found in Section 2.2, while auxiliary data sets used for comparison are presented in Section 2.3. The gridding algorithm for level 2 to level 3 processing is presented in section 3.1. Section 3.2 shows the selection of best spatial resolution for GOME-2 level 3 data. The verification and validation methodology are presented in section 3.3. Section 4 presents the resulting daily and monthly level 3 products. Result for the verification and validation of GOME-2 level 3 data is presented in Section 5. Finally, Section 6 summarises our findings.

2   Instruments and data sets

The GOME-2 instruments and the operational level 2 products of each trace gas used for the generation of gridded level 3 data are described in this section. Ground-based measurements used to validate the GOME-2 level 3 products are also presented.

2.1   GOME-2 instruments

Global Ozone Monitoring Experiment 2 (GOME-2) are passive nadir viewing satellite borne spectrometers on board the European Organization for the Exploitation of Meteorological Satellites (EUMETSAT) Metop series of satellites. The Metop satellites orbit at an altitude of ∼820 km on sun-synchronous orbits with 29 days (412 orbits) repeat cycle and a local equator overpass time of 09:30 LT (local time) on the descending node. Metop-A, the first Metop satellite, was launched on 19th October 2006. Metop-B was launched 6 years later on 17th September 2012. The third Metop satellite, Metop-C, was launched on 7th November 2018. A more detailed introduction of the Metop series of satellites can be found in Klaes et al. (2007).

The GOME-2 instruments are optical spectrometers equipped with scanning mirrors which enable across-track scanning in nadir and sideways viewing for polar coverage (Callies et al., 2000). Each GOME-2 instrument consists of four detectors covering a wavelength range of 240 - 790 nm with spectral resolution ranging from 0.26 nm to 0.51 nm. Additionally, two polarization components are measured with polarization measurement devices (PMDs) using 30 broadband channels covering the full spectral range at higher spatial resolution. The nominal spatial resolution of the instruments is 80 km (across-track) × 40 km (along-track) for the forward scan and the spatial resolution reduced to 240 km (across-track) × 40 km (along-track) for the backward scan. The scanning swath width of the GOME-2 instruments is about 1920 km. After the GOME-2 instrument on board the Metop-B satellite (refers as GOME-2B from hereafter) went in tandem operation with Metop-A in July 2013, the across-track spatial resolution of the GOME-2 instrument on board the Metop-A satellite (refers as GOME-2A from hereafter) was doubled to 40 km with the spatial coverage of a swath reduced to 960 km. The spatial resolution and coverage of GOME-2B remains unchanged. A more detailed description of the GOME-2 instruments can be found in Munro et al. (2016). Table 1 summarized the major characteristics of all three GOME-2 instruments.

Table 1. Summary of the GOME-2 instrument characteristics.

Sensor	GOME-2A	GOME-2B	GOME-2C
Operational Period	Jan 2007 - Nov 2021	Dec 2012 - Present	Jan 2019 - Present
Spectral Range	240 - 790 nm	240 - 790 nm	240 - 790 nm
Ground Pixel Resolution	80 km × 40 km / 40 km × 40 km[a]	80 km × 40 km	80 km × 40 km
Swath Width	1920 km / 960 km[a]	1920 km	1920 km
Equator Crossing Time	9:30 (local time)	9:30 (local time)	9:30 (local time)
Global Coverage	1.5 days	1.5 days	1.5 days
Level 2 Processor	GDP 4.8	GDP 4.8	GDP 4.9[*]

[a] since tandem operation with GOME-2B on 15th July 2013

[*] The GDP 4.9 was introduced for GOME-2C and includes updated instrument specific retrieval settings for NO_2 and SO_2. For NO_2, the alternative DOAS fitting-window 430.2 - 465 nm is used (because of calibration issues for GOME-2C for wavelengths <430 nm). For SO_2, improved DOAS fitting settings are used and the wavelength region has been changed to 312 - 325 nm (Valks et al., 2019).

2.2 Operational GOME-2 level 2 data

2.2.1 Total column ozone

Ozone (O_3) is an important trace gas in the Earth's atmosphere. In the stratosphere, ozone absorbs ultraviolet radiation from the sun, thus protecting the biosphere from harmful radiation (Eleftheratos et al., 2013; Hegglin et al., 2015). In the lower troposphere, natural ozone has an equally important beneficial role, because it initiates the chemical removal of air pollutants and greenhouse gases from the atmosphere such as carbon monoxide (CO), nitrogen oxides (NO_x), and methane (CH_4). However, ozone at high concentration can also be harmful to humans, plants, and animals. In addition, ozone is a greenhouse gas contributes to the warming of the Earth's atmosphere. In both the stratosphere and the troposphere, ozone absorbs infrared radiation emitted from Earth's surface, trapping heat in the atmosphere. As a result, increases or decreases in stratospheric or tropospheric ozone induce a climate forcing (Hegglin et al., 2015).

The retrieval of total column ozone from GOME-2 (ir)radiance spectra is based on the typical two step approach for weak absorbing trace gas. The first step is to apply the differential optical absorption spectroscopy (DOAS) technique (Platt and Stutz, 2008) to the GOME-2 (ir)radiance spectra within the wavelength range of 325 - 335 nm to retrieve ozone slant column densities (SCDs). Ozone absorption features are prominent in this wavelength range. In addition, GOME-2 measurements have high signal-to-noise and manageable interference effects from other trace gases in this wavelength band. The DOAS fits includes two ozone cross-sections at 218 K and 243 K. A NO_2 cross-section and the Ring spectrum are also included in the spectral fit.

The second step is the conversion of retrieved ozone slant column densities to vertical column densities (VCDs) using air mass factors (AMFs) (Solomon et al., 1987; Palmer et al., 2001). Vertical distribution profiles are essential a priori information used in the calculation of AMFs. The air mass factor calculation for ozone vertical column retrieval follows an iterative

approach. The algorithm uses a standard ozone profile to retrieve an initial ozone vertical column. Based on the initial result of the ozone vertical column retrieval, the algorithm selects the most appropriate a priori profile from the climatology database and uses it as a priori in the next iteration. The iterations end when the change in the retrieved vertical column is less than 0.1 % or it reaches the maximum limit of iterations. For GOME-2 total column ozone retrieval, the number of iterations is in most cases

5   smaller than 4. The radiative transfer model, LIDORT (Spurr, 2008), is used for the radiative transfer calculation of AMF with respective to the a priori ozone profile and cloud information. Cloud parameters are retrieved from GOME-2 measurements using the OCRA and ROCINN algorithms (see section 2.2.7) and the ozone absorption inside and below the cloud is treated by the intra-cloud correction term, which is a function of solar zenith angle and cloud albedo. AMFs are computed at a single wavelength of 325.5 nm (Van Roozendael et al., 2006). As the major part of ozone is in the stratosphere which is well above

10 clouds, therefore, all measurements (cloudy and clear sky) are used in the level 3 product. More details of the GOME-2 total column ozone retrieval can be found in Loyola et al. (2011); Hao et al. (2014).

2.2.2   Total and tropospheric column nitrogen dioxide

Nitrogen dioxide (NO_2) plays an important role in atmospheric chemistry and air quality in the troposphere. It is an air pollutant affecting human health and ecosystems. Furthermore, NO_2 in the troposphere is a major ozone precursor, while being a catalyst

15 of stratospheric ozone depletion processes which is very important for climate change studies, due to its indirect effect on the global climate (Shindell et al., 2009).

The retrieval of total and tropospheric column NO_2 from GOME-2 follows the typical two step approach for a weak absorbing trace gas. The DOAS approach is applied to GOME-2 (ir)radiance spectra to determine NO_2 slant column densities at wavelength range of 425 - 450 nm (Valks et al., 2011) for GOME-2/Metop-A and GOME-2/Metop-B (GDP 4.8). NO_2 absorp-

20 tion structures are prominent and the interference effects are manageable within this spectral window. In addition, GOME-2 measurements have high signal-to-noise in this wavelength band. For GOME-2/Metop-C (GDP 4.9), an alternative fitting-window 430.2 - 465 nm is used, as there are systematic structures in the DOAS fitting residual for GOME-2C for wavelengths <430 nm, which result in a large positive bias of ∼30 %. A single NO_2 reference cross-section spectrum at 240 K (Vandaele et al., 2002), and the interfering species ozone, O_4 and H_2O as well as Ring spectrum are included in the DOAS spectral

25 retrieval. The temperature dependence of NO_2 absorption cross-section has been taken into account in the air mass factor calculation to improve the accuracy of the retrieved columns.

The initial total VCD is retrieved assuming an unpolluted troposphere. Therefore, the air mass factor is weighted toward to stratospheric NO_2, whereas the tropospheric NO_2 amount is assumed to be negligible. This assumption is valid over large parts of the Earth, but in areas with significant tropospheric NO_2, the total column densities are underestimated and need to

30 be corrected. The air mass factors are calculated at the mid-point of the spectral fitting window at 437.5 nm using the radiative transfer model LIDORT. A harmonic climatology of stratospheric NO_2 profiles is used in the air mass factor calculation to incorporate the seasonal and latitudinal variation of stratospheric NO_2. Stratospheric NO_2 columns are estimated using the spatial filtering approach (Wenig et al., 2004; Valks et al., 2011). This method masks out potentially polluted areas and then applying a low-pass filter in the zonal direction to derive the stratospheric component. The tropospheric NO_2 vertical columns

are then derived from the residual tropospheric slant columns using a more accurate tropospheric air mass factors which considers the effects of clouds and NO_2 profile from chemistry transport model. The derived tropospheric columns are used to correct the initial total NO_2 columns under polluted conditions to provide estimate of total vertical columns.

Monthly average NO_2 profiles during GOME-2 overpass time from the chemistry transport model MOZART-2 are used in the tropospheric air mass factor calculations. Cloud properties derived from GOME-2 using the OCRA and ROCINN algorithms (see section 2.2.7) are used in the calculation of air mass factors in case of (partly) cloudy conditions. The CAL model included in OCRA/ROCINN has also been implemented in our prototype GOME-2 NO_2 algorithm, as described in Liu et al. (2020). The new NO_2 algorithm uses an improved directionally dependent Lambertian-equivalent reflectivity (DLER) for AMF calculation. It is planned to implement the prototype GOME-2 NO_2 algorithm in a future version of the operational GDP processor. The calculation of AMF for (partly) cloudy conditions uses the independent pixel approximation. For measurements over cloudy scenes, the cloud-top is usually well above the NO_2 pollution in the boundary layer. When the clouds are optically thick, the enhanced tropospheric NO_2 concentrations cannot be detected by the satellite which can result in large errors. Therefore, GOME-2 measurements with cloud radiance fraction >50 % are flagged in the level 2 data and filtered in the computation of level 3 tropospheric NO_2 product. More details of the GOME-2 total and tropospheric column NO_2 retrieval can be found in Valks et al. (2011).

2.2.3 Total column water vapour

Water vapour is one of the major components in the atmosphere with strong impacts on climate and weather. Due to its abundance in the atmosphere, making it the most important natural greenhouse gas, accounting for more than 60 % of the greenhouse effect (Clough and Iacono, 1995; Kiehl and Trenberth, 1997). The knowledge of the spatio-temporal distribution of water vapour over the globe is essential for weather prediction and climate assessments. Improving the understanding of variability and changes in water vapour is vital, especially considering that, in contrast to most other greenhouse gases, the distribution of water vapour is highly variable due to its short atmospheric lifetime.

The GOME-2 operational total column water vapour (TCWV) algorithm is based on the DOAS and AMF approach. The DOAS retrieval of water vapour slant columns is performed in the wavelength interval of 614 - 683 nm. Compared to other water vapour retrieval methods, this approach focuses only on the differential absorptions, and therefore, less sensitive to instrument changes or instrument degradation issues. The algorithm consists of three basic steps (1) DOAS fit for slant column retrieval, (2) non-linearity absorption correction of slant columns and (3) slant to vertical column conversion using AMF (Wagner et al., 2003, 2006).

The DOAS fit for water vapour retrievals takes into account O_2 and O_4 cross-sections, in addition to that of water vapour. Three types of vegetation spectra (Wagner et al., 2007), a synthetic Ring spectrum, and inverse solar spectrum are included in the DOAS fit to improve the broadband filtering and to correct for possible offsets, e.g. caused by instrumental stray light. The retrieved water vapour slant columns are then corrected for the non-linearities arising from the fact that the fine structure water vapour absorption lines are not spectrally resolved by the GOME-2 instruments. The corrected water vapour slant columns are divided by the "measured" AMFs to convert to vertical column. The "measured" AMF is defined as the ratio between

the measured O_2 slant column retrieved at the same wavelength band and the known O_2 vertical column from the standard atmosphere. This simple approach has the advantage that it corrects in first order for the effect of albedo variation, aerosol load and cloud cover without the use of additional independent information. It is also important to note that, the GOME-2 water vapour product does not rely on additional information, except for the use of an albedo database for the AMF correction. The surface albedo used for the correction is taken from monthly albedo database derived from GOME-1 observations (Koelemeijer et al., 2003) for high latitude (>50°), and SCIAMACHY observations (Grzegorski, 2009) at mid and low latitudes (<40°). For the transition between 40° and 50°, both products are interpolated linearly. This serves the aim to derive a climatologically relevant time series of TCWV measurements (Wagner et al., 2006; Lang et al., 2007; Noël et al., 2008). The current version of GOME-2 TCWV retrieval does not account for the terrain effect with elevated surface in the AMF correction, i.e. over high mountain areas (>1000 m), and the retrieval errors in TCWV are significantly higher. Therefore, these measurements are flagged and not being used in the level 3 data processing.

GOME-2 measurements significantly contaminated by clouds are also flagged in the level 2 and filtered in the level 3 products. The cloud flag in the water vapour product is set based on two indicators. The first cloud flag is set if the retrieved O_2 slant column is below 80 % of the maximum O_2 slant column for the respective solar zenith angle (roughly when about 20 % from the column to ground is missing). Especially for low and medium high clouds, the relative fraction of the column shielded by clouds for O_2 and water vapour can be very different. The second cloud flag is set if cloud fraction and cloud top albedo exceeds 0.6. More details of the GOME-2 total column water vapour retrieval can be found in Grossi et al. (2015).

2.2.4 Total column bromine monoxide

Bromine monoxide (BrO) in the lower stratosphere is involved in chain reactions that deplete ozone (Wennberg et al., 1994), while in the troposphere BrO changes the oxidizing capacity through the destruction of ozone. In particular, large amounts of BrO are often observed in the polar boundary layer during spring-time (Platt and Wagner, 1998; Richter et al., 1998), known as "bromine explosion", and lead to severe tropospheric ozone depletion by autocatalytic reactions. In addition to polar sea ice regions, enhanced BrO concentrations were also detected over salt lakes/marshes (Hebestreit et al., 1999; Hörmann et al., 2016), in the marine boundary layer, and in volcanic plumes (Theys et al., 2009; Hörmann et al., 2013).

The GOME-2 total BrO retrieval is also a typical DOAS and AMF algorithm. The DOAS retrieval of BrO slant columns is applied to the spectral range of 332 - 359 nm which covers five BrO absorption peaks and minimized the interference from other trace gases, especially formaldehyde (Theys et al., 2011). This fitting window can also minimize other artefacts due to instrument noise, viewing angle dependency and interference from incomplete ring effect correction.

The instrumental degradation of GOME-2 has negative influences on the spectral fit and results in higher residuals. Thus, affecting the noise level in the BrO columns, and the average slant columns values. Therefore, an equatorial offset correction is applied on a daily basis to the BrO data (Richter et al., 2002). This correction reduces the influences of the instrumental degradation on the total BrO column time series. Averaged BrO slant columns in the tropical latitudinal band between ±5° are calculated on a daily basis, assuming small equatorial BrO columns with no significant seasonal variations. These averaged slant columns are then subtracted from all slant columns and a constant equatorial slant column offset of 7.5×10^{13} molec/cm^2 is

added. Corrected BrO slant columns are then converted to vertical columns by using AMFs. In the GOME-2 total column BrO retrieval, AMFs are calculated at 344 nm (mid-point of DOAS fitting range) using the radiative transfer model LIDORT (Spurr, 2008). Monthly climatology BrO profiles from the chemistry transport model SLIMCAT (Chipperfield, 1999; Bruns et al., 2003) are used in the AMF calculations. In case of (partly) cloudy cases, GOME-2 cloud properties determined with the OCRA

5 and ROCINN algorithms (see section 2.2.7) are used to calculate the air mass factors in association with the independent pixel approximation. As BrO has major contribution from the stratosphere which is usually above clouds, therefore, all measurements (cloudy and clear sky) are used in the level 3 product. More details of the GOME-2 total column BrO retrieval can be found in Theys et al. (2011).

2.2.5 Total column formaldehyde

10 Formaldehyde (HCHO) is an intermediate product of the oxidation of almost all volatile organic compounds (VOCs). There-fore, it is widely used as an indicator of non-methane volatile organic compounds (NMVOCs) (Fried et al., 2011). VOCs also have significant impacts on the abundance of hydroxyl (OH) radicals in the atmosphere, which is the major oxidant in the tro-posphere. Major HCHO sources over continents include the oxidation of VOCs emitted from plants, biomass burning, traffic and industrial emissions. Oxidation of methane (CH_4) emitted from the ocean is the main source of HCHO over water and

15 pristine continental areas.

The GOME-2 total HCHO column retrieval algorithm also follows the two steps approach with DOAS retrieval of HCHO slant columns and subsequently converts the slant columns to vertical columns by using AMFs. To reduce the interference between HCHO and BrO absorption features, a two-step DOAS retrieval of HCHO slant columns is used (De Smedt et al., 2012). The first step is to determine BrO slant columns with a larger fitting window of 332 - 359 nm which includes five BrO

20 absorption peaks and effectively minimized the cross-correlation between BrO and HCHO. The retrieved BrO slant columns are then fixed in the subsequent DOAS retrieval of HCHO slant columns in the spectral band of 328.5 - 346 nm.

Although the DOAS fit settings are optimized to minimize interference from other factors, there are still unresolved spectral absorption interferences between HCHO and BrO and results in obvious zonally and seasonally dependency. In order to reduce the impact of the artefacts, an absolute normalisation is applied to HCHO slant columns on a daily basis using the reference

25 sector method (Khokhar et al., 2005). The reference sector is chosen over the Pacific Ocean (Longitude: $140°$ - $160°$W), where the only source of HCHO is the oxidation of CH_4 which can be reproduced by model simulation quite well. The mean HCHO slant column density in the reference sector is determined by a polynomial fit, which is then subtracted from the retrieved slant columns on this day, and replaced by a HCHO background value taken from IMAGES version 2 chemistry transport model simulations (Müller and Stavrakou, 2005).

30 Corrected HCHO slant columns are then converted to vertical columns by using AMFs. HCHO AMFs are calculated at 335 nm using the radiative transfer model LIDORT. Monthly averaged profiles taken from chemistry transport model (CTM) IMAGES version 2 simulation in 2007 are used as a priori HCHO profiles in the AMF calculations. The IMAGES version 2 model simulations are in a horizontal resolution of $2.0°$ (latitude) $\times$ $2.5°$ (longitude), with 40 vertical layers extending from the surface up to $\sim$44 hPa. In case of the presence of clouds, cloud properties derived by the OCRA and ROCINN

algorithms (see section 2.2.7) are used to calculate the air mass factors using the independent pixel approximation. For cloudy scene measurements, clouds are usually above the boundary layer where the major part of HCHO is located. If the clouds are optically thick, HCHO below cloud cannot be detected by the satellite and results large uncertainties. Therefore, measurements with cloud radiance fraction >50 % are flagged and not being used in the level 3 data processing. More details of the GOME-2

5   total column HCHO retrieval can be found in De Smedt et al. (2012).

2.2.6   Total column sulphur dioxide

Sulphur dioxide (SO_2) is an important trace species playing key role in atmospheric chemistry on both local and global scales through the formation of sulphate aerosols and sulphuric acid. The impacts of SO_2 range from short-term pollution to climate forcing. SO_2 emits to the atmosphere through both natural and anthropogenic processes. About one-third of the global sulphur

10   emissions originate from natural sources (volcanoes and biogenic dimethyl sulphide), the major contributors to the total budget are anthropogenic emissions through the combustion of fossil fuels (coal and oil) and smelting.

The GOME-2 SO_2 retrieval algorithm also follows the two steps approach with DOAS retrieval of SO_2 slant columns and subsequently converts the slant columns to vertical columns by using AMFs. The DOAS algorithm for SO_2 is based on the DOAS fit settings dedicated for ozone retrieval with adjustments to optimize for SO_2 retrieval (Rix et al., 2009, 2012). The

15   DOAS fit for the retrieval of SO_2 slant column is applied to the wavelength range of 315 - 326 nm for GOME-2/Metop-A and -B (GDP 4.8) and 312 - 325nm for GOME-2/Metop-C (GDP 4.9).

The background level of atmospheric SO_2 is very low over large parts of the Earth. To account for any systematic bias in the retrieved total column SO_2 and to ensure a geospatial consistency of the results, a background correction is applied to the data to avoid non-zero columns over regions known to have very low SO_2 and at high solar zenith angles. The background correction

20   scheme calculates offset SO_2 slant columns based on latitude and surface height information. This offset is calculated on a daily basis with measurements binned to 2° resolution in latitude. In addition, the offset values are calculated separately at 5 surface altitude bins. Median offset values based on the calculated offset values in the last two weeks before the day of interest is used as the corresponding offset SO_2 slant columns to minimize the influences from outliers or missing data in the daily dataset. This latitude and altitude dependent value is then subtracted from the SO_2 slant column derived from the DOAS retrieval.

25   Corrected SO_2 slant columns are then converted to vertical columns by using AMFs. The major challenge in the SO_2 retrieval is that the vertical distribution of SO_2 in the atmosphere is usually unknown. Depending on the type of emission, SO_2 can be located from the ground up to the stratosphere. In the GOME-2 SO_2 retrieval, it assumes two scenario (1) volcanic eruption emissions and (2) anthropogenic sources. For volcanic emission scenario, the AMFs are calculated assuming the SO_2 plume follows a Gaussian profile shape with central plume height at 15.0 km, 6.0 km and 2.5 km above sea level. For anthropogenic

30   emissions, the AMFs are calculated assuming a homogeneous layer from surface up to 1 km. The GOME-2 SO_2 product typically refers to the volcanic scenario with assumed plume height at 6 km. The AMF is calculated at 320 nm (GOME-2A and GOME-2B) and 313 nm (GOME-2C) using the radiative transfer model LIDORT. For scenarios in the presence of clouds, GOME-2 cloud properties determined with the OCRA and ROCINN algorithms are used to calculate the air mass factors.

2.2.7 Cloud parameters

It is very important to derive cloud properties from GOME-2 observations as clouds significantly affects the retrieval of tropospheric trace gases. The most predominant effect of clouds in trace gas retrieval is that they shield the trace gas absorption below clouds. However, clouds can also enhance the absorption due to multiple scattering within the cloud. The GOME-2 retrieval of the trace gases vertical columns assumes independent pixel approximation (IPA) for cloudy scene measurements. For tropospheric species, i.e., tropospheric NO_2, water vapour, HCHO, especially in the case of low clouds and large cloud fractions, the presence of clouds can result in large errors. Therefore, measurements with high cloud cover are flagged in these products and being filtered in the level 3 process.

The optical cloud recognition algorithm (OCRA) and retrieval of cloud information using neural network (ROCINN) algorithms (Loyola et al., 2007; Lutz et al., 2016) are used to obtain cloud information from GOME-2 observations. Clouds are treated as reflecting Lambertian surfaces in the algorithm and cloud information is reduced to the specification of three parameters: cloud fraction, cloud-top albedo and cloud-top pressure. The radiometric cloud fraction is retrieved from the broad-band polarization of UVN measurements (UV-VIS-NIR) by OCRA, while effective cloud pressure and cloud albedo are retrieved by ROCINN from observations in the oxygen A-band (O_2-A) around 760 nm. The OCRA algorithm separates each measurement to two components: a cloud-free background and a residual contribution describing the influence of clouds. The key to the algorithm is the construction of a cloud-free composite that is invariant with respect to atmosphere, to topography and to solar and viewing geometries. The effective cloud fraction is determined by examining the separation between the reflectance measured by the PMDs of GOME-2 and their cloud-free composite values. Note that OCRA is also sensitive to scattering by aerosols present in a given GOME-2 scene. Therefore, the retrieved cloud fraction also includes the aerosol effects. Furthermore, the GOME-2 cloud algorithm has been improved to distinguish clouds for measurements affected by sun-glint over ocean, which is a common phenomenon that occur at the edges of the GOME-2 swath. The detection of cloud over sun-glint is achieved by analyzing the broad-band polarization measurements (Loyola et al., 2011; Lutz et al., 2016). Noted that the OCRA/ROCINN algorithm recently has been upgraded to include the retrieval of cloud-top height and cloud optical thickness using the Clouds-As-Layers (CAL) model (Loyola et al., 2018) and this new feature has been implemented to process TROPOMI data. We are also planning to implement the new feature to GOME-2 operational GDP processor in the future (see section 2.2.2).

The cloud fraction derived from OCRA is then ingested by ROCINN as fixed input (Loyola et al., 2007), which derived cloud-top height and cloud albedo using measurements at the O_2-A band. In the radiative transfer simulations, oxygen absorption in the earthshine spectra including the reflection from Earth's surface and cloud-top is considered in the atmospheric radiative transfer. Surfaces are assumed to be Lambertian reflectors. Black-sky albedo climatology from the MEdium Resolution Imaging Spectrometer (MERIS) is used as input for the radiative transfer and in ROCINN version 3. Radiative transfer simulations in ROCINN include Rayleigh scattering and polarization. High-resolution reflectances computed with VLIDORT (Spurr, 2006) are used to create a complete data set of simulated reflectance for all viewing geometries and geophysical scenarios, and for various combinations of cloud fraction, cloud-top height and cloud-top albedo. The inversion is performed using neural network techniques. The cloud-top height retrieved by ROCINN is converted to cloud-top pressure assuming a U.S.

standard atmosphere (Anderson et al., 1986). The retrieved cloud properties are then used in the subsequent processing of trace gas column retrieval and provided in the corresponding level 3 products.

2.3 Validation data sets

2.3.1 Brewer ozone measurements

5 Brewer ozone data are obtained the World Ozone and Ultraviolet Radiation Data Center (WOUDC, http://www.woudc.org). The WOUDC data center is part of the Global Atmosphere Watch (GAW) programme of the World Meteorological Organization (WMO), providing quality-assured Brewer measurements. Brewer instruments measure intensity at several wavelength intervals in the UV band. Total column ozone is retrieved from the relative intensities among these UV channel. Brewer ozone data has long been used to validate satellite observations of ozone (Balis et al., 2007a, b; Antón et al., 2009; Loyola et al., 2011;

10 Koukouli et al., 2012, 2015; Garane et al., 2018, 2019). In this study, we only use the direct sun Brewer observations of total column O_3 for the validation of GOME-2 level 3 product.

2.3.2 ZSL-DOAS and MAX-DOAS NO_2 measurements

Zenith-Scattered-Light Differential Optical Absorption Spectroscopy (ZSL-DOAS) data are obtained from the Network for the Detection of Atmospheric Composition Change (NDACC). NDACC ZSL-DOAS network provides total column NO_2 obser-

15 vations with standardized operating procedures and harmonized retrieval methods. ZSL-DOAS data from NDACC stations is available on the NDACC data host facility (see http://www.ndacc.org). ZSL-DOAS measurements during twilight periods are sensitive to stratospheric absorbers due to the geometrical enhancement of the optical path in the stratosphere. Therefore, it has long been used for the validation of satellite total NO_2 observations (Ionov et al., 2008; Celarier et al., 2008). The retrieval of total column NO_2 from ZSL-DOAS observations is based on the Langley method, which calculates the corresponding air mass

20 factor according to its observation and solar geometry. As most of the ZSL-DOAS sites are located in relative clean regions, therefore, the major contribution of total column NO_2 is expected to be coming from the stratosphere. Due to the morning overpass time of GOME-2, ZSL-DOAS observations of total column NO_2 during the morning twilight period are used to validate GOME-2 level 3 total NO_2 products. As the measurement time of GOME-2 and ZSL-DOAS are nigh, therefore, these data are comparable without the need of photochemical correction.

25 The Multi-AXis Differential Optical Absorption Spectroscopy (MAX-DOAS) is a passive remote sensing technique which uses spectroscopic observations of scattered sunlight at different viewing zenith angles to derive column densities of trace gas. Due to its compact experimental setup and high sensitivity to lower troposphere, it has been widely used for the validation of satellite observations of tropospheric column NO_2 (Brinksma et al., 2008; Celarier et al., 2008; Irie et al., 2008, 2009, 2012, 2016; Ma et al., 2013; Kanaya et al., 2014; Chan et al., 2015, 2018, 2019, 2020b; Drosoglou et al., 2017; Wang et al., 2017;

30 Compernolle et al., 2020; Pinardi et al., 2020a; Verhoelst et al., 2021). Ground-based MAX-DOAS instruments are operated by various research institutes around the world, and the data is centrally managed by BIRA-IASB within the context of NItrogen Dioxide and FORmaldehyde VALidation (NIDFORVAL). The affiliation of MAX-DOAS instruments in the NDACC network

is still under progress, following efforts done in the NORS, QA4ECV and ESA's FRM4DOAS project to harmonize and automatize data processing. In this study, MAX-DOAS observations of tropospheric column NO_2 are used to validate GOME-2 level 3 tropospheric NO_2 products.

2.3.3 Sun-photometer water vapour measurements

5 The AERosol RObotic NETwork (AERONET) uses CIMEL CE-318 sun-photometers to measure direct sun and sky radiance at multiple wavelengths (Holben et al., 1998). These sun-photometer observations do not only provide information of aerosol optical properties (Holben et al., 2001) but also of columnar water vapour content (Alexandrov et al., 2009). Water vapour columns are retrieved from sun-photometer observations in the near infrared (NIR) at 940 nm where water vapour absorption is rather strong. The inversion of water vapour columns is based on the attenuation of radiation through the atmosphere. A

10 more detailed description of the water vapour retrieval algorithm can be found in Alexandrov et al. (2009). In total, there are over 1000 AERONET stations around the globe providing columnar water vapour observations and they have been used extensively for satellite validation (Bennouna et al., 2013; Diedrich et al., 2015; Martins et al., 2019; Chan et al., 2020a; Garane et al., 2022). The AERONET water vapour product has also been validated by microwave radiometry, GPS and radiosondes measurements (Pérez-Ramírez et al., 2014). The sun-photometer measurements are in general underestimating the columnar

15 water vapour by 6 - 9 % (Pérez-Ramírez et al., 2014). In this study, cloud screened and quality assured level 2.0 data are used to validate GOME-2 level 3 total column water vapour products.

2.3.4 ZSL-DOAS BrO measurements

The ZSL-DOAS observations at Harestua (60.22 °N, 10.75 °E), Norway are used to validate the GOME-2 level 3 total column BrO product. ZSL-DOAS observation of total BrO columns are photochemically corrected to the GOME-2 overpass time

20 (9:30 local time). The operation of the ZSL-DOAS instrument and the retrieval of BrO column are performed by BIRA-IASB. Detailed description of the ZSL-DOAS instrument setup and BrO column retrieval algorithm can be found in Hendrick et al. (2007).

2.3.5 MAX-DOAS HCHO measurements

Ground-based MAX-DOAS observations are used to validate GOME-2 level 3 total column HCHO product. MAX-DOAS

25 observations show very good sensitivity in the troposphere where most of the HCHO resides. Therefore, it has long been used for satellite validation (Vigouroux et al., 2009; Li et al., 2013; De Smedt et al., 2015b, 2021; Wang et al., 2017; Chan et al., 2019, 2020b; Kumar et al., 2020). The retrieval of HCHO columns from MAX-DOAS observations are performed within a wavelength range similar to the GOME-2 retrieval, i.e., 328 - 359 nm. Ground-based MAX-DOAS instruments are operated by various research institutes around the world, and the data is centrally managed by BIRA-IASB within the context

30 of NIDFORVAL.

2.3.6 Pandora SO$_2$ measurements

The Pandonia Global Network is a direct-sun spectrometer network used to monitor trace gas worldwide. The Pandora instrument is used to measure columnar amounts of trace gases in the atmosphere. Pandora determines trace gas amounts from direct-sun observations by using the DOAS technique with theoretical solar spectrum as a reference. As the anthropogenic SO$_2$ emission has been reduced significantly in the recent decades, the background SO$_2$ level is mostly zero around the globe and only few locations with signification anthropogenic SO$_2$ sources. Considering the low background SO$_2$ level and the high measurement noise of SO$_2$ data, it is more appropriate to validate the satellite observations over locations with significant variation and sources. Mexico City is one of the few places with significant anthropogenic SO$_2$ sources. Therefore, we use the Pandora SO$_2$ observations at Mexico City to validate GOME-2 level 3 total column SO$_2$ products.

3 Methodology

3.1 Gridding algorithm

GOME-2 level 3 data products are developed with the aim of providing easily translatable data sets to both facilitate scientific progress (e.g. on climate trend analysis and low-frequency climate variability) and satisfy public interest. The processing of GOME-2 level 3 data requires binning of the level 2 data onto a regular 2-dimensional latitude-longitude grid.

The binning of level 2 data to regular latitude-longitude grid includes taking the arithmetic mean and standard deviation of all level 2 data points falling onto the grid cell in a given period, i.e., a day or a month, with possible trimming of low-quality measurements due to large spectral fit residual and cloud contamination for tropospheric species, i.e., tropospheric NO$_2$, water vapour and HCHO. For all species, only forward-scan pixels are used in the gridding process. In case of cloudy measurements, most of the tropospheric gases, i.e., tropospheric NO$_2$, water vapour and HCHO, are mainly situated below clouds, while satellite observations could not measure the part below cloud and result in large uncertainties. Therefore, these measurements are not used in the production of level 3 data. For stratospheric species, i.e., total column O$_3$, NO$_2$, BrO and SO$_2$, no cloud filtering is applied.

Several gridding routines have been developed to create global and regional maps of trace gas distribution, e.g., Wenig et al. (2008); Chan et al. (2012); Kuhlmann et al. (2014). These gridding algorithms typically assume that measurement values are constant within the satellite pixel boundaries. This assumption is considered sufficient for creating global maps. More sophisticated approach uses parabolic spline method to interpolated adjacent satellite pixels to create high resolution (e.g., 1 km $\times$ 1 km) regional maps (Kuhlmann et al., 2014). As GOME-2 ground pixel size is relatively large, a significant grid effect would be induced by assigning each GOME-2 measurement to a single grid cell based on their center coordinates of the GOME-2 ground pixel, without taking into account the pixel geometry and extension. Therefore, the gridding process considers the overlapping area of the GOME-2 ground pixel and the latitude-longitude grid. For grid cells partially overlapped with the satellite pixel, the percentage of overlap (satellite pixel fully covers the entire grid cell is considered as 100 % overlap) is calculated and used as weighting for the calculation of mean value, uncertainty and standard deviation. Figure 1 shows an
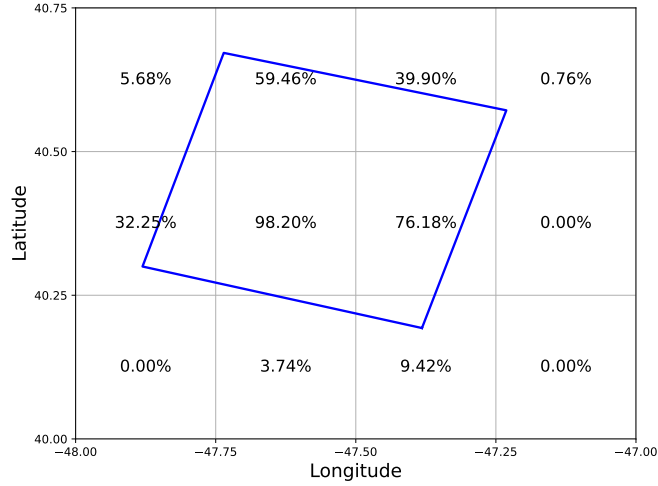
Figure 1. A GOME-2A ground pixel (blue) overlaid on a $0.25° \times 0.25°$ latitude-longitude grid (gray). The percentage of overlap (weighting) for each grid box is indicated.

example of the calculation of the weighting (percentage of overlap) for grid boxes overlapping with a GOME-2A ground pixel. The gridded columns can be expressed as Eq. 1.

$$VCD_g = \frac{\sum_{i=1}^{n} VCD_i \times w_i}{\sum_{i=1}^{n} w_i} \tag{1}$$

where VCD_g is the gridded trace gas column while VCD_i represents each individual satellite measurement (partly) overlap-
5 ping with the grid cell. The weighting is denoted as w which is the percentage of the grid cell covered by the satellite pixel. The weighting or the number of observations is also included in the level 3 product. The uncertainty of gridded columns can be express as Eq. 2.

$$E_g = \sqrt{\frac{\sum_{i=1}^{n} E_i^2 \times w_i^2}{\sum_{i=1}^{n} w_i^2}} \tag{2}$$

where E_g is the uncertainty of gridded trace gas column while E_i represents the uncertainty of each individual measurement.
10 The standard deviation of gridded columns can be express as Eq. 3.

$$\sigma_g = \sqrt{\frac{\sum_{i=1}^{n} VCD_i^2 \times w_i^2}{\sum_{i=1}^{n} w_i^2} - \left(\frac{\sum_{i=1}^{n} VCD_i \times w_i}{\sum_{i=1}^{n} w_i}\right)^2} \tag{3}$$

where σ_g is the standard deviation of gridded trace gas column.

3.2 Sampling resolution

The processing of GOME-2 level 3 data requires binning of the level 2 data onto a regular 2-dimensional latitude-longitude grid. The selection of appropriate resolution of the latitude-longitude grid is essential for the production of level 3 products. On one hand, it is important to preserve the original spatial features captured in the level 2 data with higher spatial resolution,
5 but on the other hand, it is necessary to keep the data files in a reasonable size to be user friendly.

To select the best spatial resolution for the level 3 product, we have analyzed the binning results with various resolutions, i.e., $0.1° \times 0.1°$, $0.25° \times 0.25°$ and $0.5° \times 0.5°$. Figure 2 shows GOME-2A data of each trace gas species gridded in different resolutions and level 2 data in the original instrument resolution for an orbit over North China on 15th July 2014. Missing data are mainly due to filtering of cloudy pixels and other low-quality observations. GOME-2A data are shown due to its highest
10 spatial resolution among all three GOME-2 instruments (GOME-2A: $40\,km \times 40\,km$ after 15th July 2013, GOME-2B and C: $40\,km \times 80\,km$). We looked into the spatial smoothing/averaging effect over North China, as this region is expected to show strong spatial gradients of tropospheric pollutants, i.e., NO_2. Data in all four resolutions show very similar spatial structures. The absolute values of level 3 data are also consistent with the level 2 product. The results show gridding GOME-2 data with higher spatial resolution (i.e., $0.1° \times 0.1°$) better preserve the original GOME-2 instrument footprint, while rather strong
15 smoothing/averaging effect is observed from data gridded with lower spatial resolution (i.e., $0.5° \times 0.5°$). Although gridded data with $0.25° \times 0.25°$ resolution shows some smoothing/averaging effect, it still captures the spatial variations reasonably well.

Figure 3 shows monthly averaged GOME-2A data of each trace gas species gridded in different resolutions over North China in July 2014. Differences between data gridded with different resolutions are also shown for reference. Data gridded
20 in all three resolutions show very similar spatial structures. Hotspots of anthropogenic pollutants, i.e., tropospheric NO_2, can be clearly observed from the monthly averaged data. Species with major contribution from natural sources, e.g., O_3 and water vapour, show rather smooth appearance. Despite the fact that large numbers of observations are included in the monthly averaging process, species with lower signal to noise ratio, e.g., HCHO and SO_2, still show rather high background noise. This is mainly due to the low column density and absorption of these species. This effect is as expected more significant for
25 data gridded in higher spatial resolution, i.e., $0.1° \times 0.1°$, due to less spatial averaging. Traces of the satellite footprints can still be seen in the $0.1° \times 0.1°$ resolution monthly averaged data, while the satellite footprints are much less significant in the $0.25° \times 0.25°$ and $0.5° \times 0.5°$ resolution data. The differential plots between data gridded with $0.1° \times 0.1°$ and $0.25° \times 0.25°$ resolution in general show only very small differences. Slightly larger discrepancies mainly appear over pollution hotspots, i.e., for tropospheric NO_2. In contrast, data in $0.5° \times 0.5°$ resolution show much bigger differences from $0.1° \times 0.1°$ resolution
30 data. Compared to $0.25° \times 0.25°$ resolution data, $0.5° \times 0.5°$ resolution data shows 2 to 4 times higher underestimation of tropospheric NO_2 columns over pollution hotspots. The comparison of GOME-2 data gridded in different resolutions indicates that $0.25° \times 0.25°$ resolution is a balance to preserve the satellite resolution (GOME-2A: $40\,km \times 40\,km$, GOME-2B and C: $40\,km \times 80\,km$) while capturing the strong spatial variations for most of the tropospheric gases, i.e., NO_2, water vapour and HCHO. In addition, the data file size of level 3 products with $0.1° \times 0.1°$ resolution is about 6 times larger than that of
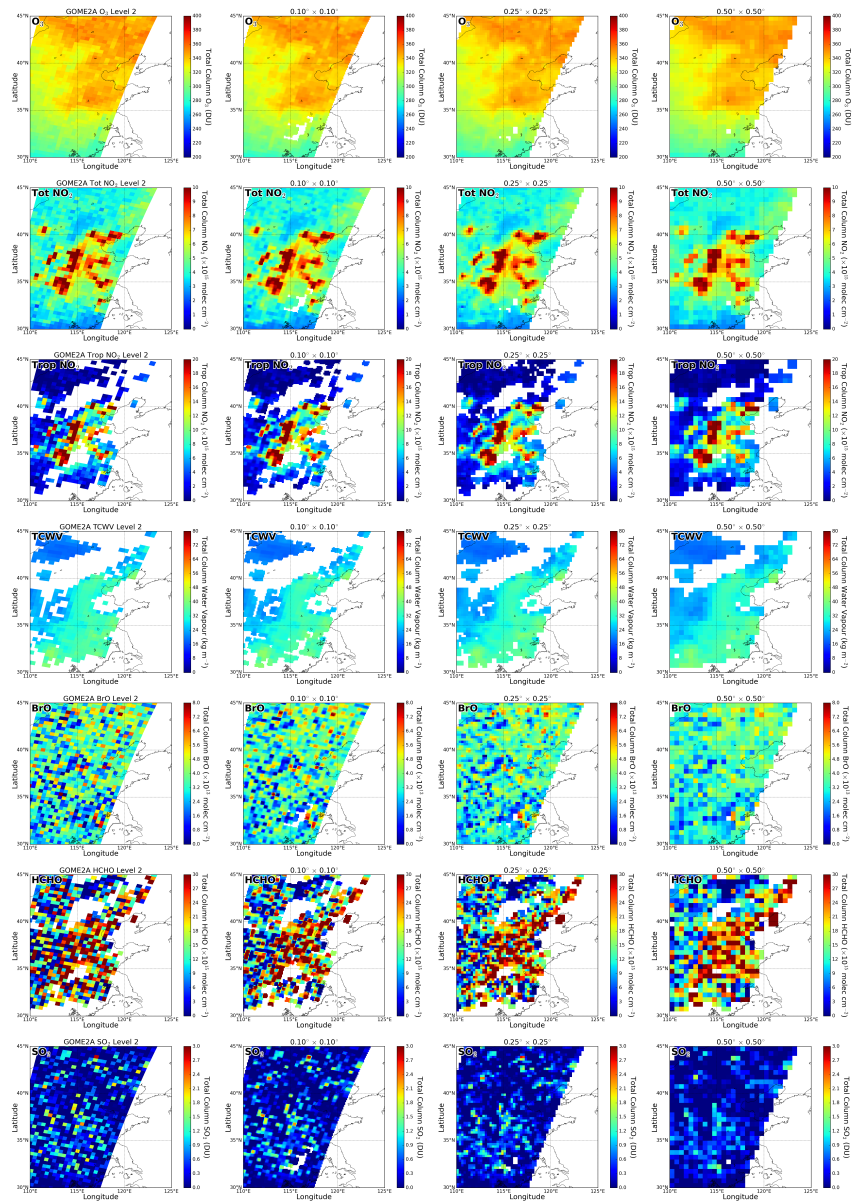
Figure 2. GOME-2A observations of total column O$_3$ (1st row), total column NO$_2$ (2nd row), tropospheric column NO$_2$ (3th row), total column water vapour (4th row), total column BrO (5th row), total column HCHO (6th row), and total column SO$_2$ (7th row). Data are shown in the original instrument resolution (1st column from the left), gridded with 0.1° × 0.1° resolution (2nd column from the left), 0.25° × 0.25° resolution (3th column from the left), and 0.5° × 0.5° resolution (column on the right). GOME-2A observations on 15 July 2014 over North China are shown. Missing data are mainly due to cloudiness.
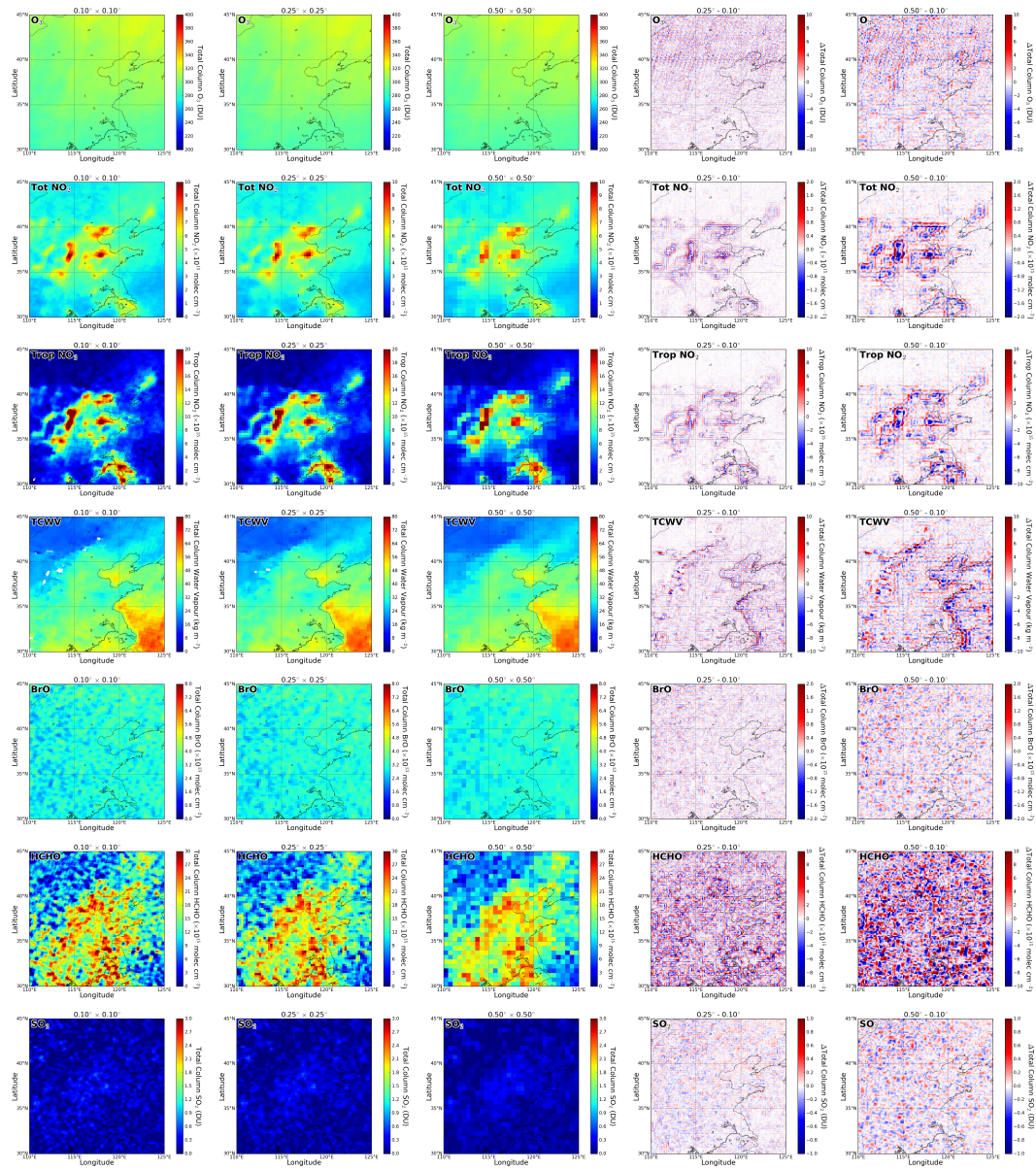
Figure 3. Monthly averaged GOME-2A observations of total column O_3 (1st row), total column NO_2 (2nd row), tropospheric column NO_2 (3th row), total column water (4th row), vapour total column BrO (5th row), total column HCHO (6th row), and total column SO_2 (7th row) over North China in July 2014. Gridded data with $0.1° \times 0.1°$ resolution (1st column from the left), $0.25° \times 0.25°$ resolution (2nd column from the left), and $0.5° \times 0.5°$ resolution (3th column from the left) are shown. Differences between $0.1°$, $0.25°$ and $0.5°$ are also shown for reference.

$0.25° \times 0.25°$, while the information content does not show significant difference, especially for monthly products. Therefore, we concluded that $0.25° \times 0.25°$ resolution is a suitable choice for GOME-2 level 3 products.

3.3 Verification and Validation Methods

The GOME-2 level 3 products are generated from the level 2 datasets which have already been fully validated (see validation reports in https://acsaf.org/valreps.php). Therefore, the verification and validation of GOME-2 level 3 product mainly focus on two major aspects, the consistency among the three GOME-2 sensors and the comparison to reference ground-based measurements. Each GOME-2 level 3 product is compared to different reference ground-based measurements, information of the reference ground-based measurements used to validate GOME-2 level 3 products are listed in Table 3.

The comparison of GOME-2 level 3 data to reference ground-based measurements requires spatial and temporal matching of the two data sets. The following criteria are applied to co-locate the GOME-2 level 3 products and ground-based reference data sets.

– The grid cell of the level 3 GOME-2 products covering the ground-based measurement site is paired with the daily/monthly ground-based measurements

– For ground-based Brewer, MAX-DOAS, sun-photometer and Pandora measurements, they are temporally averaged around the GOME-2 overpass time from 8:30 to 10:30 (local time)

– For ZSL-DOAS measurements, morning twilight period measurement is used for comparison

After co-locating the GOME-2 and ground-based datasets, we compare the GOME-2 level 3 products to reference ground-based data sets through scatter plot, histogram of the differences, and sort the differences/bias by year, latitude band or measurement site as box plot and time series to investigate the systematic bias/error.

4 GOME-2 level 3 products

The GOME-2 level 3 products are in two different temporal resolution, daily and monthly. Both daily and monthly level 3 product consists of gridded trace gas columns and other auxiliary parameters, i.e., cloud, surface and statistical parameters. The level 3 products are separated for each species (i.e., O_3, NO_2, water vapour, BrO, HCHO and SO_2) and each GOME-2 instrument (i.e., GOME-2A, B and C). All products are in a spatial resolution of $0.25° \times 0.25°$ with coordinates ranging from $180°$ W to $180°$ E in longitude and from $90°$ S to $90°$ N in latitude (720 (latitude) $\times$ 1440 (longitude) grid cell). The data are organized in a user-friendly and self-describing NetCDF-4 (Network Common Data Form) format, based upon the instrument/platform (GOME-2A/Metop-A, GOME-2B/Metop-B or GOME-2C/Metop-C) and the temporal period of collection (daily or monthly data set).

Figure 4 show examples of the daily level 3 products for all trace gases and all GOME-2 instruments, while examples of monthly level 3 data are shown in Figure 5. Missing data are mainly due to filtering of low-quality data, e.g., cloud contamination, high solar zenith angle and high spectral fit residual. The spatial coverage of GOME-2A daily product is different from
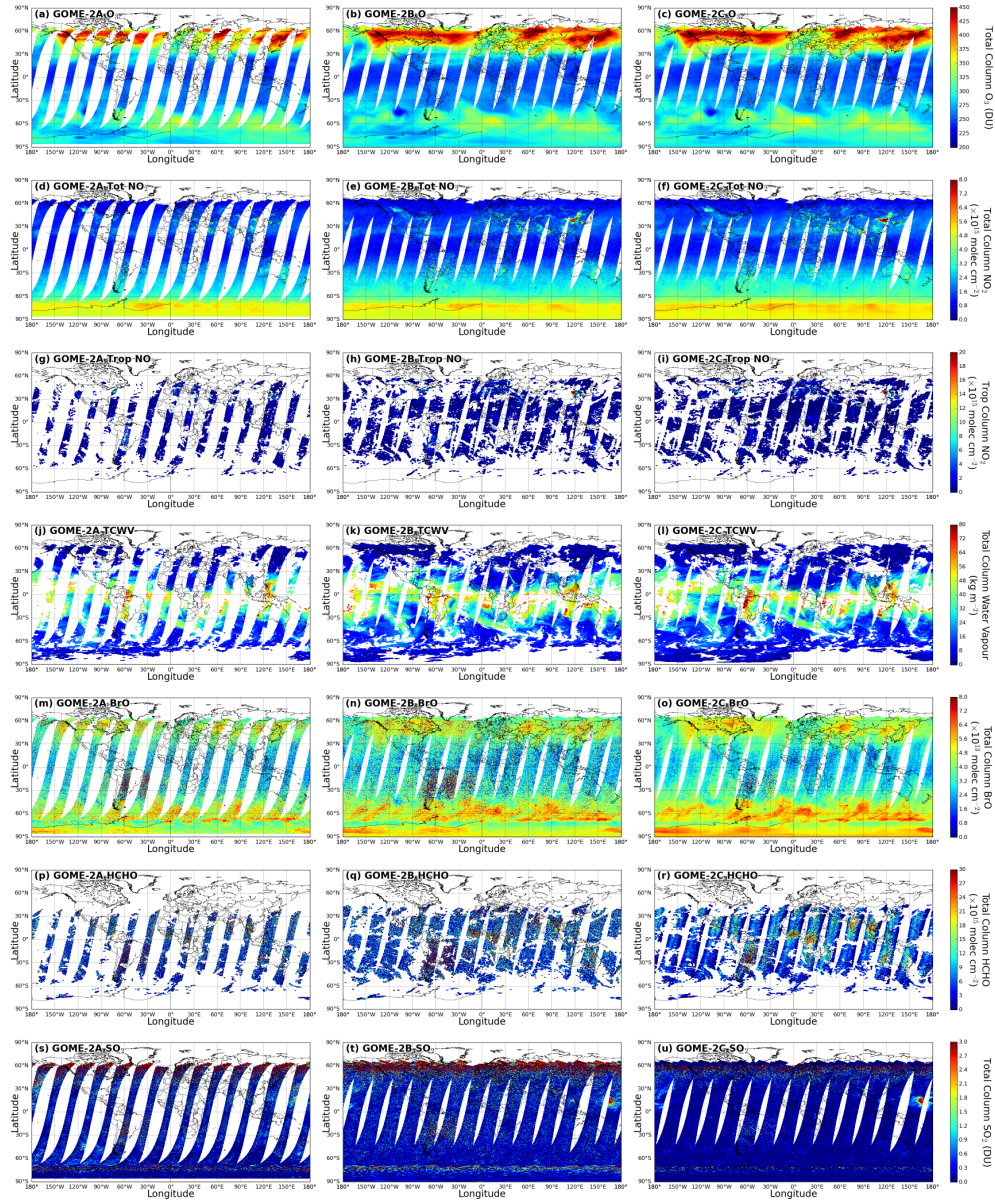
Figure 4. Daily level 3 product of GOME-2A (1st column), GOME-2B (2nd column), and GOME-2C (3th column) for 15 January 2020. Total column O_3 (1st row), total column NO_2 (2nd row), tropospheric column NO_2 (3th row), total column water vapour (4th row), total column BrO (5th row), total column HCHO (6th row), and total column SO_2 (7th row) are shown.

GOME-2B and C due to the improvement of spatial resolution after it went in tandem operation with GOME-2B in July 2013. The noise levels of monthly GOME-2A data are significantly higher than those of GOME-2B and C. This is mainly related to
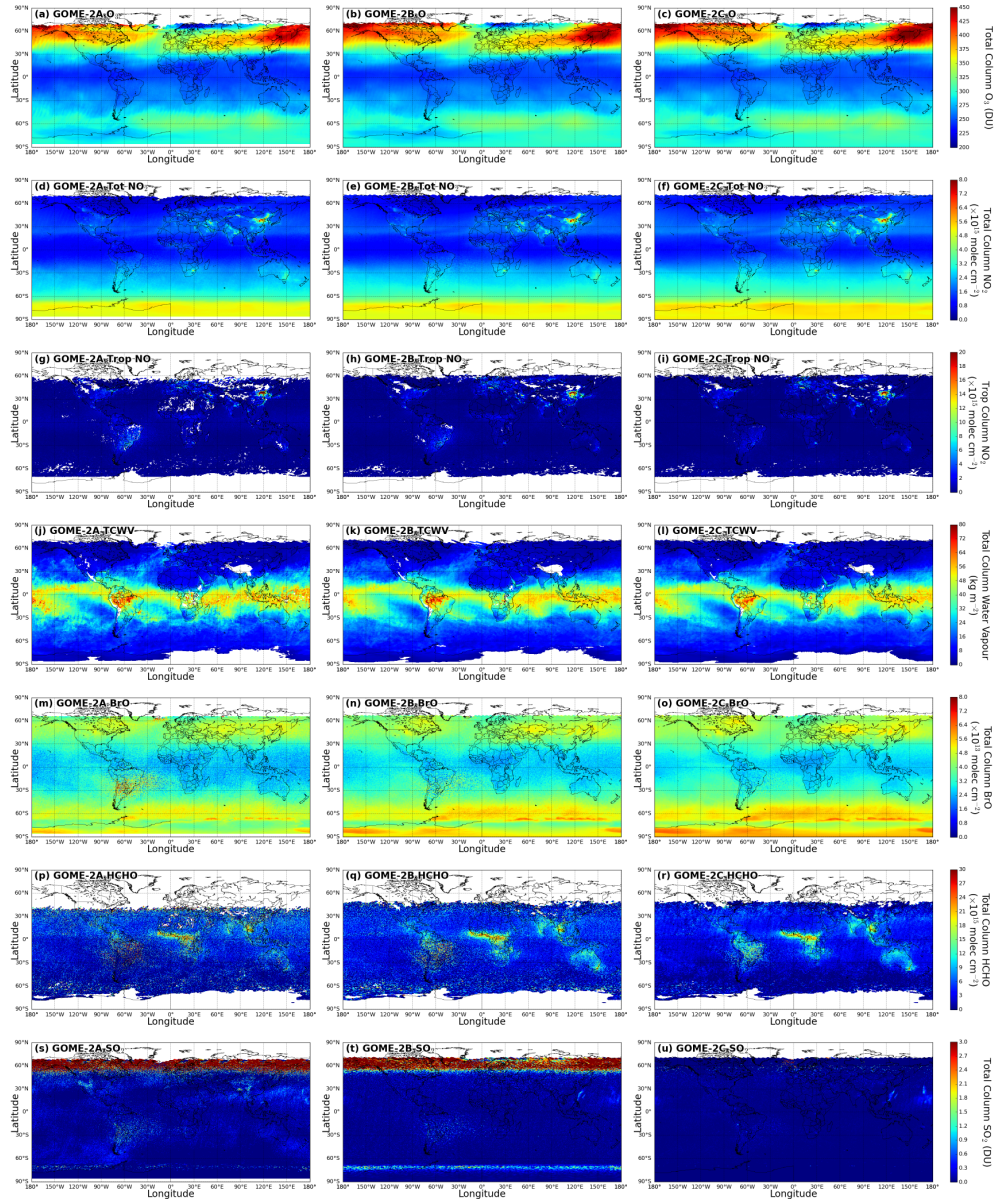
Figure 5. Monthly level 3 product of GOME-2A (1st column), GOME-2B (2nd column), and GOME-2C (3th column) for January 2020. Total column O$_3$ (1st row), total column NO$_2$ (2nd row), tropospheric column NO$_2$ (3rd row), total column water vapour (4th row), total column BrO (5th row), total column HCHO (6th row), and total column SO$_2$ (7th row) are shown.

less spatial averaging and instrument aging. This effect is particularly obvious for species with lower signal to noise ratio, e.g.,

HCHO and SO$_2$. In addition, the stripe pattern is also more significant for GOME-2A, e.g., water vapour product, due to the narrower swath width of GOME-2A measurements.
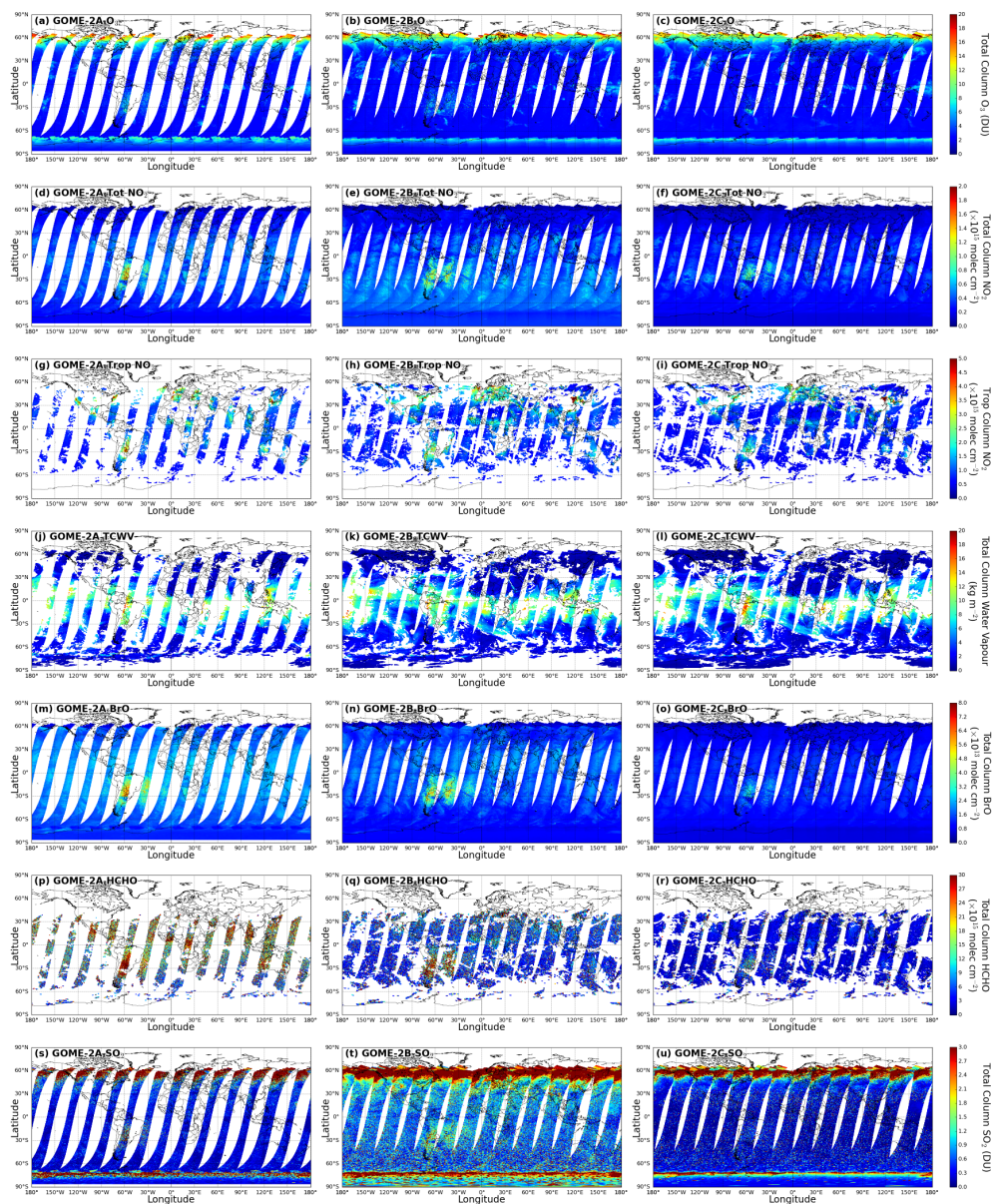
Figure 6. Derived measurement errors in the daily level 3 product of GOME-2A (1st column), GOME-2B (2nd column), and GOME-2C (3th column) for 15 January 2020. Measurement errors of total column O$_3$ (1st row), total column NO$_2$ (2nd row), tropospheric column NO$_2$ (3th row), total column water vapour (4th row), total column BrO (5th row), total column HCHO (6th row), and total column SO$_2$ (7th row) are shown.
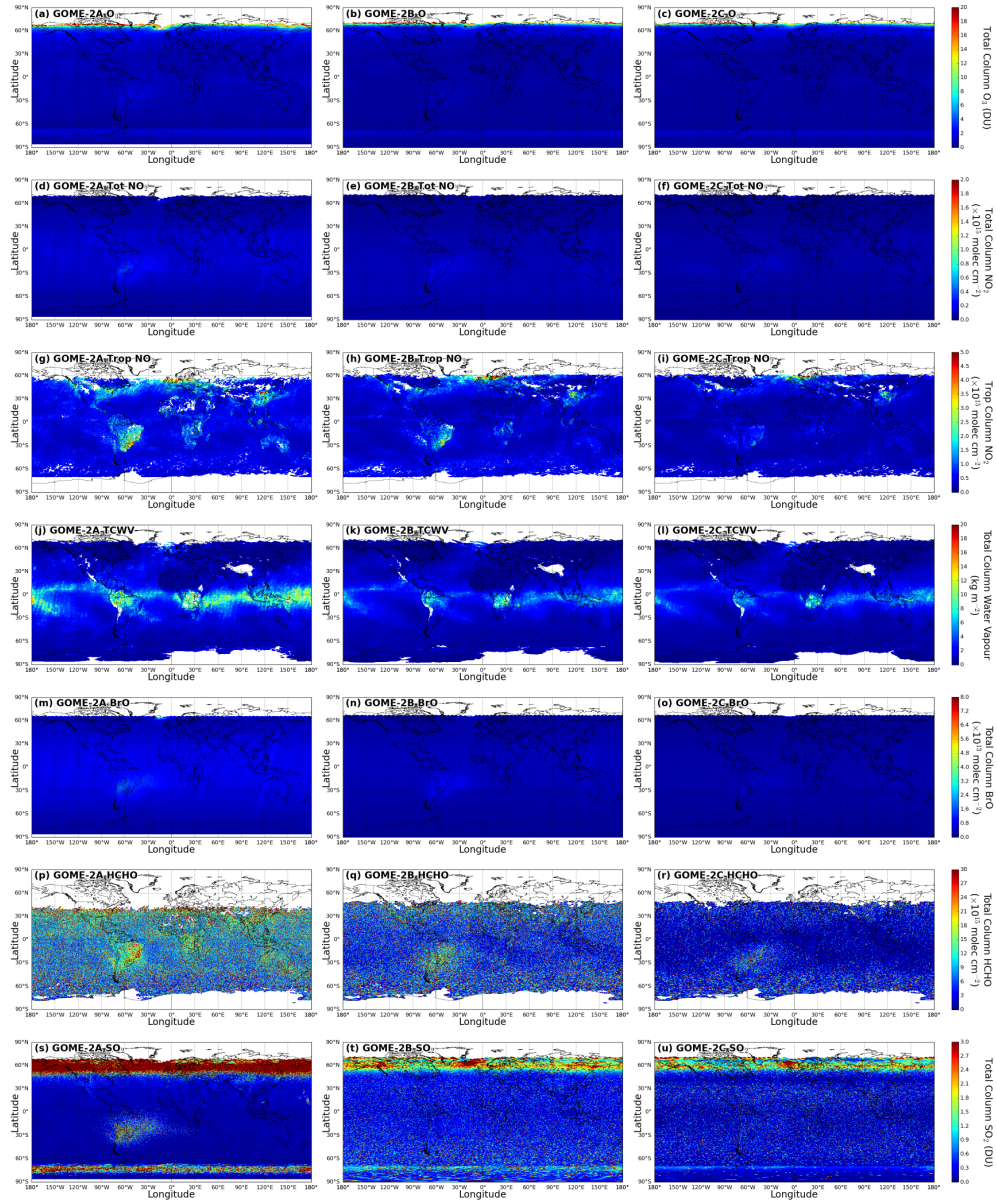
Figure 7. Derived measurement errors in the monthly level 3 product of GOME-2A (1st column), GOME-2B (2nd column), and GOME-2C (3th column) for January 2020. Measurement errors of total column O_3 (1st row), total column NO_2 (2nd row), tropospheric column NO_2 (3th row), total column water vapour (4th row), total column BrO (5th row), total column HCHO (6th row), and total column SO_2 (7th row) are shown.

Figure 6 and 7 show examples of derived measurement errors in the daily and monthly level 3 products for all trace gases and all GOME-2 instruments. The measurement errors are in general related to the instrument noise, a-priori assumption in

the AMF calculations, cloud effect and climatological input parameters, such as surface albedo and pressure profile. Some of the terms are multiplicable, such as AMF, and therefore they are higher where the columns are higher. For measurement with lower signal to noise ratio, such as HCHO and SO_2, the measurement errors increase significantly in the polar regions where the radiance intensities are low as they are observed with higher solar zenith angles. The inclusion of measurement error in the level 3 products provides addition information on the measurement accuracy and users can use it as indicator to make additional filtering of the data.

Figure 8 and 9 show examples of the standard deviation in the daily and monthly level 3 products for all trace gases and all GOME-2 instruments. The standard deviation in most area (except the polar regions) in the daily products is expected to be close to zero as there is only overlapping with neighboring pixels measured at roughly the same of the day. While standard deviation over polar regions is expected to be higher as there are multiple measurements at different time of the day. The standard deviation in the monthly products reflects both the instrument/measurement noise and the natural variability. Higher standard deviations of SO_2 columns over the polar regions are related to the low signal to noise ratio for observations taken with high solar zenith angles. In addition, the standard deviations of NO_2, BrO, HCHO and SO_2 are higher over South America mainly due to high cloudiness. While the standard deviation of O_3 and water vapour columns are mainly driven by their natural variability. The standard deviation in the level 3 products provides addition information on the measurement precision and natural variability. Depending on the propose, users can use it to filter the data or study the variability.

5   Validation

In this section, we present validation results of the GOME-2 level 3 products. The GOME-2 level 3 products are first examined with respect to their cross-sensor consistency. In addition, level 3 products of each trace gas are compared to ground-based observations for validation.

5.1   Cross-sensors consistency

5.1.1   Average and bias

Figure 10 shows the global monthly mean time series of (a) total column O_3, (b) total column NO_2, (c) tropospheric column NO_2, (d) total column water vapour, (e) total column BrO, (f) total column HCHO and (g) total column SO_2 for GOME-2A, B and C. The error bars represent the 1σ standard deviation of variation. All species except for SO_2 show pronounced seasonal variation patterns. The seasonal patterns are related to the natural variability and the variation of coverage area of the GOME-2 measurements.

The global monthly mean total column O_3 time series of GOME-2A, B and C are mostly overlapping with each other, indicating the good agreement among the three sensors. However, GOME-2C is reporting a slightly higher (2 - 3 DU) value compared to GOME-2A and B. This is likely related to the small difference in instrument characteristic, e.g., scan angle dependency and polarization sensitivity.
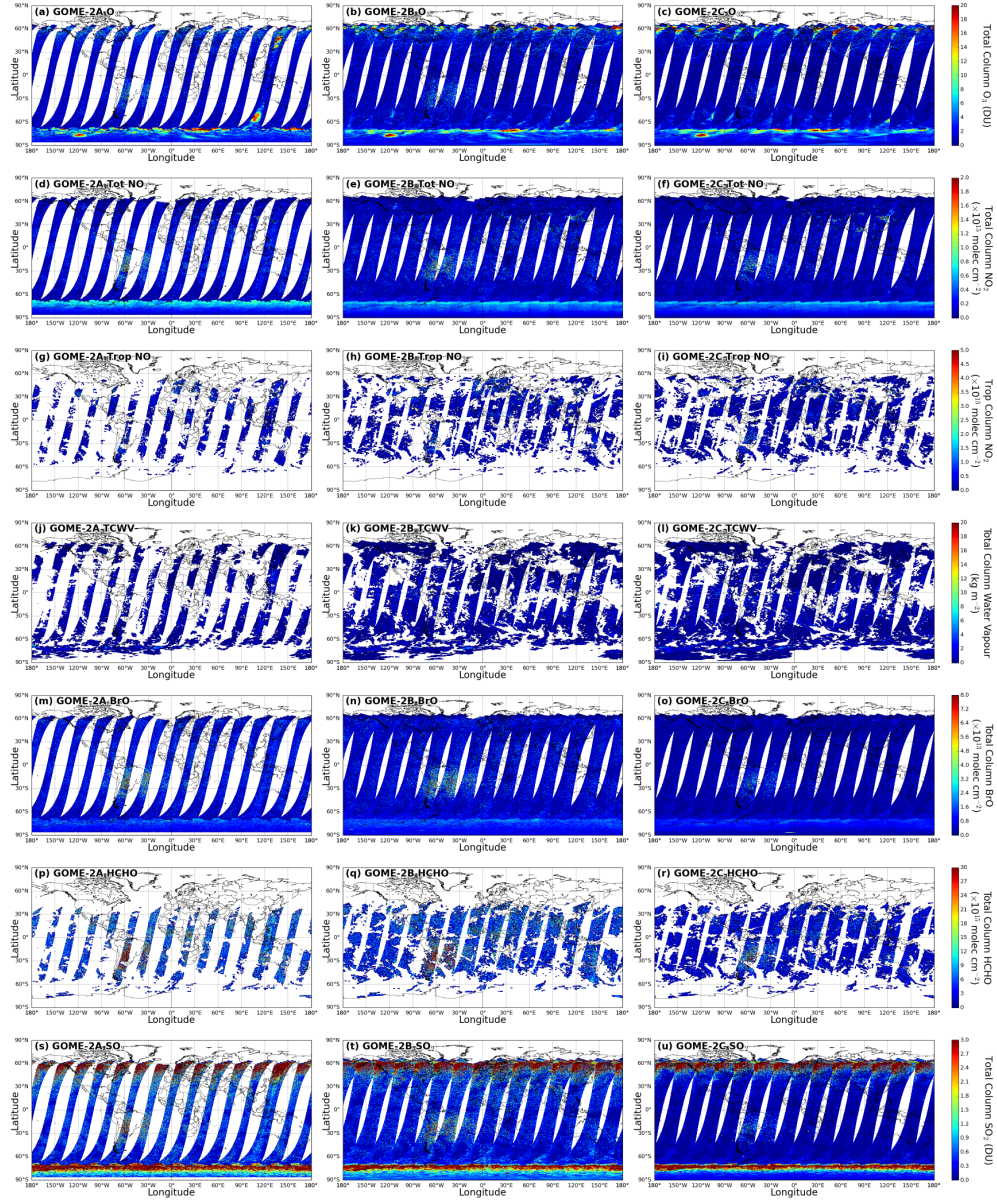
Figure 8. Derived standard deviation in the daily level 3 product of GOME-2A (1st column), GOME-2B (2nd column), and GOME-2C (3th column) for 15 January 2020. Standard deviation of total column O_3 (1st row), total column NO_2 (2nd row), tropospheric column NO_2 (3th row), total column water vapour (4th row), total column BrO (5th row), total column HCHO (6th row), and total column SO_2 (7th row) are shown.

For total column NO_2, observations from GOME-2A and B show very good consistency, while GOME-2C data are about 1.2×10^{14} molec cm^{-2} higher than that of GOME-2A and B. Tropospheric column NO_2 from GOME-2A and B are also in
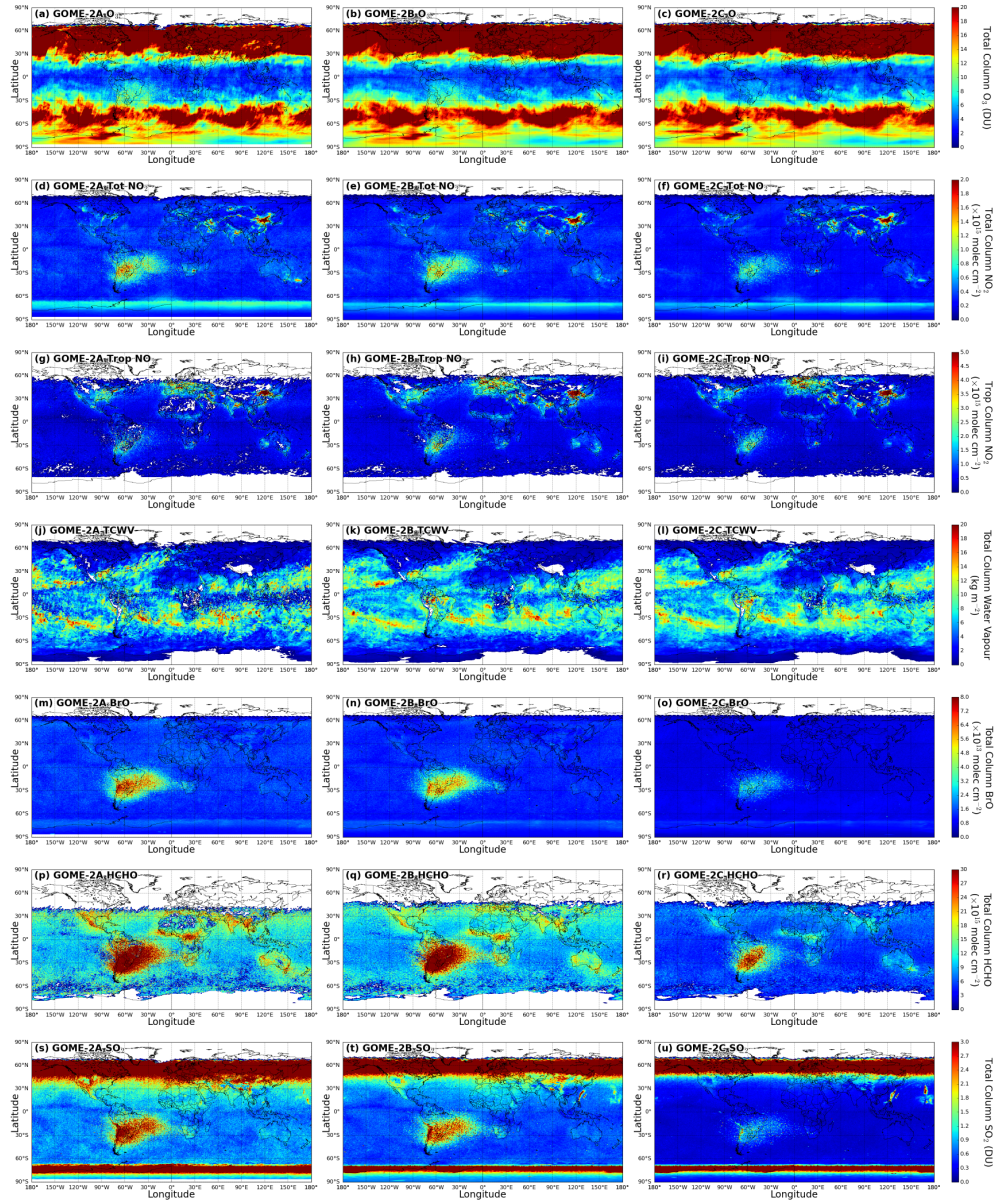
Figure 9. Derived standard deviation in the monthly level 3 product of GOME-2A (1st column), GOME-2B (2nd column), and GOME-2C (3th column) for January 2020. Standard deviation of total column O_3 (1st row), total column NO_2 (2nd row), tropospheric column NO_2 (3th row), total column water vapour (4th row), total column BrO (5th row), total column HCHO (6th row), and total column SO_2 (7th row) are shown.

good agreement. However, GOME-2C observations are about 1.5×10^{14} molec cm^{-2} lower than GOME-2A and B observations. The discrepancies in NO_2 observations is likely related to the different processor versions (GDP 4.8 for GOME-2A
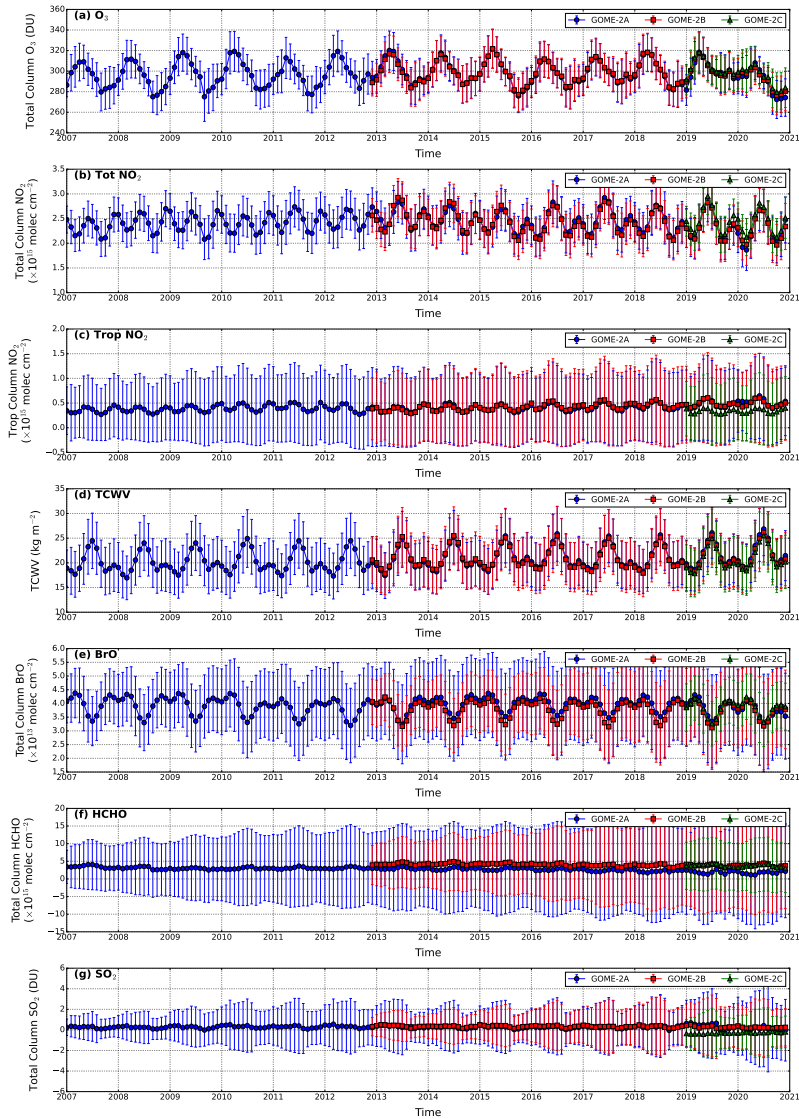
Figure 10. Time series of global monthly mean (a) total column O_3, (b) total column NO_2, (c) tropospheric column NO_2, (d) total column water vapour, (e) total column BrO, (f) total column HCHO and (g) total column SO_2 for GOME-2A (blue lines), GOME-2B (red lines) and GOME-2C (green lines). The error bars represent the 1σ standard deviation variation.

and B and GDP 4.9 for GOME-2C). The spectral fitting band of NO_2 is slightly different in different processor version (see Section 2.2.2). Previous validation study shows that the NO_2 slant columns retrieved from GOME-2C observations are slightly higher than that of GOME-2B (Pinardi et al., 2019), indicating the impact of the different spectral fitting bands on the NO_2 retrieval. In addition, the positive bias in the GOME-2C total column NO_2 shows an impact on the tropospheric columns in

the stratospheric and tropospheric separation process (Pinardi et al., 2019), and result in the discrepancies in the tropospheric columns.

Total column water vapour measurements from all three GOME-2 sensors also show very good consistency with bias smaller than $1\,\mathrm{kg\,m^{-2}}$.

5 For BrO observations, GOME-2B measurements show a negative bias of ~ 1.0 - 1.5×10^{12} molec cm^{-2} compared to GOME-2A and C. The discrepancies are partly related to the difference in the scanning swath width and the scan angle dependency (Merlaud et al., 2020). The impact of scan angle dependency on BrO measurements is more significant for GOME-2C compared to GOME-2B, which is likely linked to the polarization sensitivity of the GOME-2C instrument (Merlaud et al., 2020).

GOME-2A observations of total column HCHO are in general 1.5 - 1.9×10^{12} molec cm^{-2} lower than GOME-2B and C 10 measurements. Lower HCHO columns are observed by GOME-2A over Amazon, Central Africa, Southeast Asia and Australia (see Figure 5), thus result in slightly lower global averages. Similar to BrO measurements, the scan angle dependency issue is also reported to be significant for GOME-2C HCHO observations (Pinardi et al., 2020b). The scan angle dependency effect can also be seen in the BrO and HCHO daily level 3 product.

Total column SO_2 observations from GOME-2C are in general $0.5\,\mathrm{DU}$ lower than GOME-2A and B, result in a slightly 15 negative global average. Higher global average of SO_2 observed by GOME-2A and B is related to the extreme values taken with high solar zenith angle thus low signal to noise ratio (see Figure 4 and 5), while this effect is much less significant for GOME-2C. The overall bias and root mean square of error among the GOME-2 sensors for each product are summarized in Table 2.

Table 2. Bias and root mean square error of trace gas columns among the three GOME-2 sensors.

Species (unit)	GOME-2B - GOME-2A[a]		GOME-2C - GOME-2A[b]		GOME-2C - GOME-2B[b]	
	Bias	RMSE	Bias	RMSE	Bias	RMSE
Total O_3 (DU)	0.22 ± 2.24	5.13 ± 1.52	3.36 ± 3.68	7.41 ± 2.52	2.29 ± 0.81	4.60 ± 1.00
Total NO_2 ($\times 10^{13}$ molec cm^{-2})	-2.35 ± 6.31	14.54 ± 2.17	12.05 ± 7.56	18.91 ± 5.79	12.70 ± 3.84	16.33 ± 2.83
Tropo NO_2 ($\times 10^{13}$ molec cm^{-2})	0.69 ± 2.94	63.38 ± 23.37	-15.96 ± 4.93	77.22 ± 11.92	-14.86 ± 3.59	67.05 ± 38.71
TCWV (kg m^{-2})	-0.14 ± 0.36	3.15 ± 0.34	-0.93 ± 0.22	3.35 ± 0.42	-0.52 ± 0.09	2.32 ± 0.30
Total BrO ($\times 10^{12}$ molec cm^{-2})	-1.41 ± 1.25	5.34 ± 1.03	0.52 ± 1.45	6.22 ± 0.59	1.02 ± 0.40	3.37 ± 0.30
Total HCHO ($\times 10^{15}$ molec cm^{-2})	1.54 ± 0.41	8.24 ± 2.19	1.89 ± 0.54	11.00 ± 2.11	-0.08 ± 0.28	5.68 ± 0.55
Total SO_2 (DU)	0.06 ± 0.13	1.21 ± 0.46	-0.53 ± 0.34	2.20 ± 0.51	-0.56 ± 0.14	2.08 ± 0.51

[a] for period from 2013 to 2021

[b] for period from 2019 to 2021

5.1.2 Zonal average

20 Each GOME-2 monthly averaged level 3 product derived from all three sensors is sorted by latitude and plotted in Figure 11.
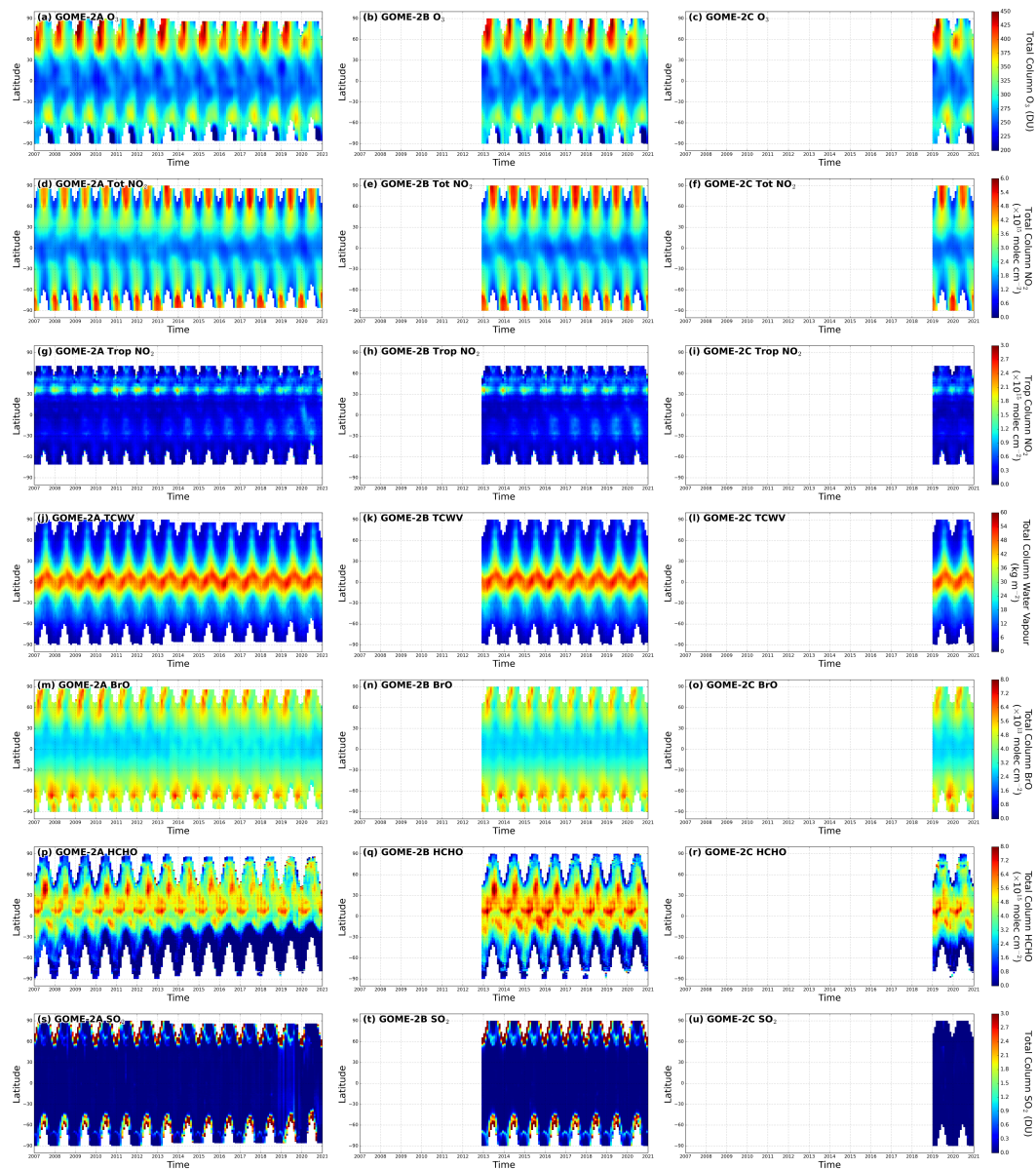
Figure 11. Monthly zonal average of total column O_3 (1st row), total column NO_2 (2nd row), tropospheric column NO_2 (3th row), total column water vapour (4th row), total column BrO (5th row), (total column HCHO (6th row) and total column SO_2 (7th row). Data from GOME-2A (1st column from the left), GOME-2B (2nd column from the left) and (3th column from the left) are shown.

All three GOME-2 sensors show consistent zonal and seasonal O_3 patterns. Higher O_3 columns are observed over high latitudes, and lower values are found over the tropics. Total column O_3 over the Arctic shows a peak in February to March and a minimum in August to October, while Antarctica displays a reverted seasonal pattern.

Both total and tropospheric column NO_2 from all three GOME-2 sensors show good zonal and seasonal consistency. Elevated total column NO_2 are observed in the polar regions during the warm months. This seasonal pattern is attributed to the stratospheric variation of NO_2. Compared to total column NO_2, tropospheric column NO_2 shows a very different zonal and seasonal pattern. Tropospheric NO_2 is mostly concentrated at the mid-latitudes of the northern hemisphere. It is because most of the population are living in this part of the world, thus higher emissions occur at this latitude band. Tropospheric NO_2 at mid-latitudes also shows a seasonal pattern with higher values over winter, which is related to higher energy consumption and longer atmospheric lifetime of NO_2 during the cold months. A significant increasing trend of tropospheric NO_2 was observed by GOME-2A and B over the sub-tropics and mid-latitudes of the southern hemisphere in the recent years (see Figure 11g and h). GOME-2C observed a much less significant enhancement of tropospheric NO_2 in the southern hemisphere, which leads to lower global average tropospheric NO_2 measured by GOME-2C. This discrepancy is likely related to the difference in retrieval wavelength and the subsequent stratosphere and troposphere separation process.

Total column water vapour observations from all three GOME-2 sensors show consistent zonal and seasonal patterns, with higher values in the tropic and lower at high latitudes. Total column water vapour is also higher during the warm months of the corresponding hemisphere.

All three GOME-2 sensors also show very similar zonal and seasonal patterns of total column BrO. However, GOME-2A total column BrO observations from 2014 to 2019 are slightly higher than that of GOME-2B at all latitude bands and results a small bias of 1.41×10^{12} molec cm^{-2}. However, when we look into the data from 2020 to 2021, the bias is smaller and result a smaller bias of 0.52×10^{12} molec cm^{-2} with GOME-2C observations.

Total column HCHO from all three GOME-2 sensors show higher values over tropics and sub-tropics, while lower values appear at higher latitudes. Both GOME-2A and B measurements show a significant decreasing trend of HCHO in the southern hemisphere. However, GOME-2A measurements are significantly lower than GOME-2B and C, resulting a bias of -1.54 and -1.89 $\times 10^{15}$ molec cm^{-2} when compared to GOME-2B and C observations. The discrepancy is related to the underestimation over HCHO rich regions, e.g., Amazon, Australia, Southeast Asia, China and North America (see Figure 5). This bias is probably related to the background correction process.

Total column SO_2 observations from all three GOME-2 sensors show very low SO_2 levels (very close to 0) around the globe as expected. However, GOME-2A and B measurements show significantly higher noise for measurement with high solar zenith angle and result a small overestimation under these extreme observation geometries, while this effect are much less significant for GOME-2C. Therefore, GOME-2C observations are in general about 0.5 DU lower than GOME-2A and B. GOME-2A measurement is also about 0.5 DU higher in general compared to the year before and after.

5.2 Comparison to ground-based observations

In this section, each GOME-2 level 3 products are compared to the corresponding reference ground-based observations. We are looking into the scatter plot, histogram of the differences, and sort the differences/bias by year, latitude band or measurement site as box plot and time series between GOME-2 and reference data sets to investigate the systematic bias/error.

5.2.1 Total column ozone
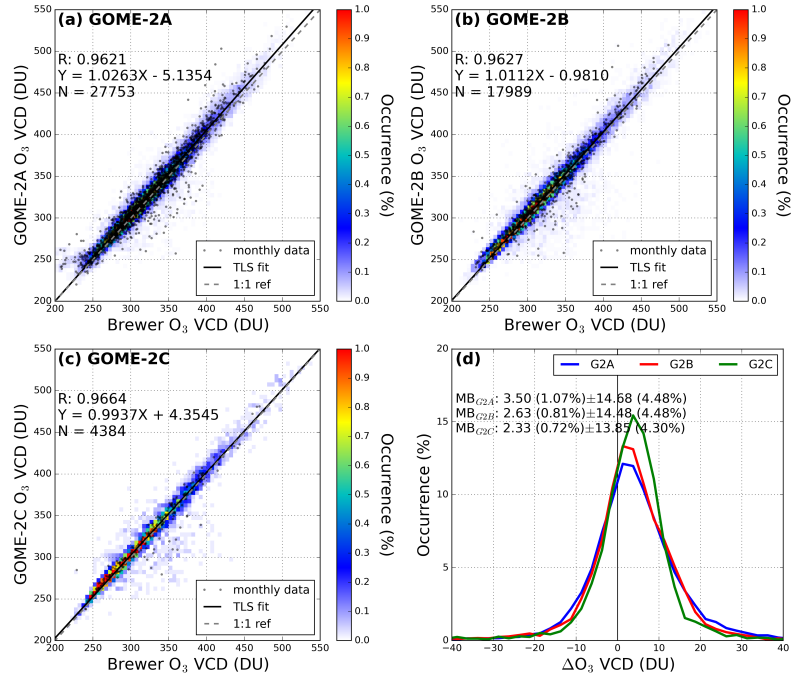
Figure 12. Comparison of daily and monthly total column O$_3$ measured by the ground-based Brewer instruments to (a) GOME-2A, (b) GOME-2B and (c) GOME-2C. Histograms of the differences of total column O$_3$ between GOME-2 and Brewer observations are shown in (d). Co-located daily and monthly averaged data are used in the comparison. Total least squares regression is based on daily data.

Daily and monthly GOME-2 level 3 total column ozone are compared to the co-located Brewer observations. Figure 12 shows the density scatter plots for the comparison of total column ozone between GOME-2 and ground-based Brewer observations. Comparisons of GOME-2A, B and C data are shown in Figure 12a, b and c, respectively. Monthly data are also shown

5   as black dots. Histograms of the differences between GOME-2 and Brewer observations are shown in Figure 12d. Scatter plots show that GOME-2 monthly data is well in line with the daily data. And the agreement between GOME-2 and Brewer is in general very good with Pearson correlation coefficient (R) of ∼0.96 for all three GOME-2 sensors. The slopes of the total least squares regression for the comparisons of all three instruments are very close to 1 (1.03 for GOME-2A, 1.01 for GOME-2B, and 0.99 for GOME-2C). The offsets of the total least squares regression range between -5.1 to 4.3 DU. In gen-

10   eral, the GOME-2 data sets show a small positive bias of 2.3 to 3.5 DU (0.72 - 1.07 %) compared to Brewer observations with standard deviation of 13.9 to 14.7 DU (4.03 - 4.48 %). The bias between all three GOME-2 sensors and ground-based Brewer observations is below 1 % which is within the uncertainty of Brewer measurements (Kerr et al., 1988) and fulfils the product requirements.
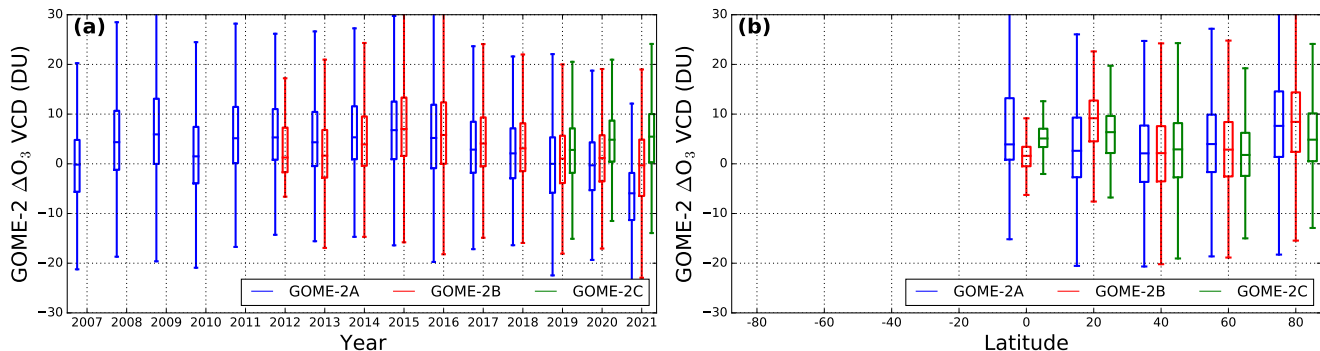
Figure 13. Comparison of total column O$_3$ between ground-based Brewer instruments and GOME-2 observations. Data are sorted by year in (a), and latitude band in (b).

Figure 13 shows box plots of the differences of total column ozone between GOME-2 level 3 product and co-located Brewer measurements. GOME-2 data is sorted by the measurement year (Figure 13a) and latitude band (Figure 13b). The box plot for the southern hemisphere is mostly empty due to insufficient number of ground-based observations. The mean difference between GOME-2 and Brewer observations are within 5 DU for most of the years. However, we observed that there are years
5 with positive bias while some years with negative bias. This is mostly related to the availability of ground-based data at different measurement sites. As some sites are bias high/low, and it will affect the statistic if they are not available for some years. On the other hand, the latitude dependent analysis shows that GOME-2 observations is consistently higher than the ground-based Brewer measurements in the Northern Hemisphere and result a positive bias of 2.3 to 3.5 DU on average. In addition, GOME-2C observations are about 2 - 3 DU higher than GOME-2A and B, which is likely relate to the instrumental issues which has
10 been mentioned in Section 5.1.1.

5.2.2 Total column NO$_2$

Daily and monthly GOME-2 level 3 total column NO$_2$ are compared to the co-located ZSL-DOAS observations. Figure 14 shows the density scatter plots for the comparison of total column NO$_2$ between GOME-2 and ground-based ZSL-DOAS observations. Comparisons of GOME-2A, B and C data are shown in Figure 14a, b and c, respectively. Monthly data are also
15 shown as black dots. Histograms of the differences between GOME-2 and ZSL-DOAS observations are shown in Figure 14d. Scatter plots show that GOME-2 monthly data is well in line with the daily data. GOME-2 level 3 total column NO$_2$ is in general agree well with ZSL-DOAS observations with Pearson correlation coefficient (R) of 0.85 to 0.88. However, GOME-2 observations are in general slightly lower than ZSL-DOAS observations. The slopes of the total least squares fit for the comparisons of all three instruments vary from 0.84 to 0.88 with offset ranging from 0.05 - 0.19 $\times 10^{15}$ molec cm^{-2}. Overall,
20 the GOME-2 level 3 total NO$_2$ products are biased low by 0.24 - 0.29 $\times 10^{15}$ molec cm^{-2} (8 - 10 %) compared to ground-based
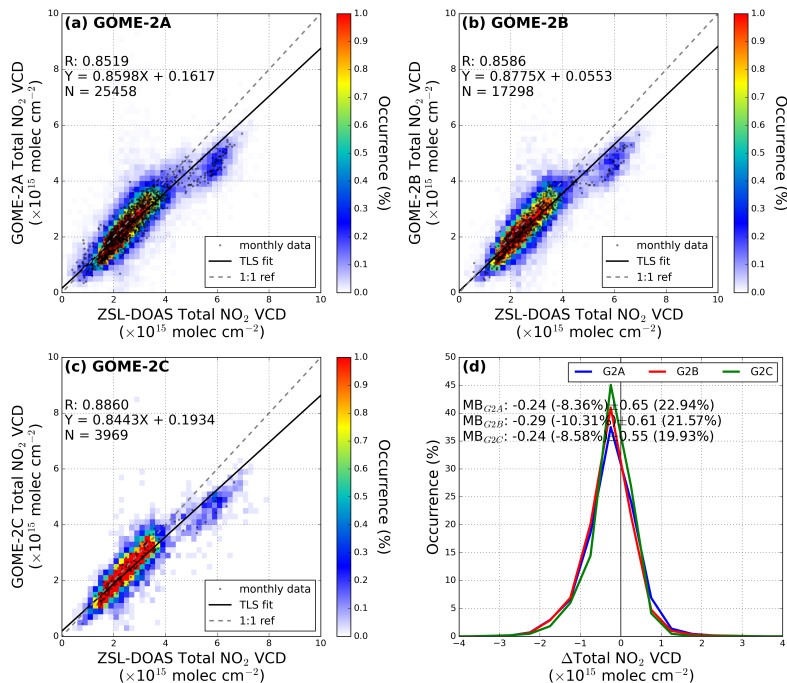
Figure 14. Comparison of daily and monthly total column NO_2 measured by the ground-based ZSL-DOAS to (a) GOME-2A, (b) GOME-2B and (c) GOME-2C. Histograms of the difference of total column NO_2 between GOME-2 and ZSL-DOAS observations are shown in (d). Co-located daily and monthly averaged data are used in the comparison. Total least squares regression is based on daily data.

ZSL-DOAS measurements. Considering that the uncertainty of satellite and ground-based measurements is about 10 %, the agreement between the two dataset is very satisfactory.

The scatter plots for all three instruments show a two clusters characteristic. The major cluster of total column NO_2 below 4×10^{15} molec cm^{-2} shows very good agreement between GOME-2 and ZSL-DOAS observations. The minor cluster at 5 -
5   6×10^{15} molec cm^{-2} shows significant underestimation of NO_2 column by 0.5 - 1.0×10^{15} molec cm^{-2} which is related to the measurement over Polar regions. Figure 15 shows the time series of total column NO_2 measured at Dumont d'Urville, Antarctica and Sodankylä, Finland. We observed that the total column NO_2 measured by GOME-2 is significantly lower than the ground-based ZSL-DOAS observations during summer months. This is because of the multiple overpasses over Polar Regions during summertime. Therefore, GOME-2 level 3 data represents the real "daily average" while ZSL-DOAS only
10 capture the morning values. Due to the diurnal variation of NO_2, it is expected that ZSL-DOAS measurements in the morning are higher than the daily averages. If we do not consider these two stations in the analysis, the minor cluster in the scatter plots would be removed. In addition, the underestimation would reduce to 0.13 - 0.21×10^{15} molec cm^{-2} (5 - 7 %).

Figure 16 shows box plots of the differences of total column NO_2 between GOME-2 level 3 product and co-located ZSL-DOAS measurements. Data are sorted by the measurement year (Figure 16a) and measurement site (Figure 16b). The mean
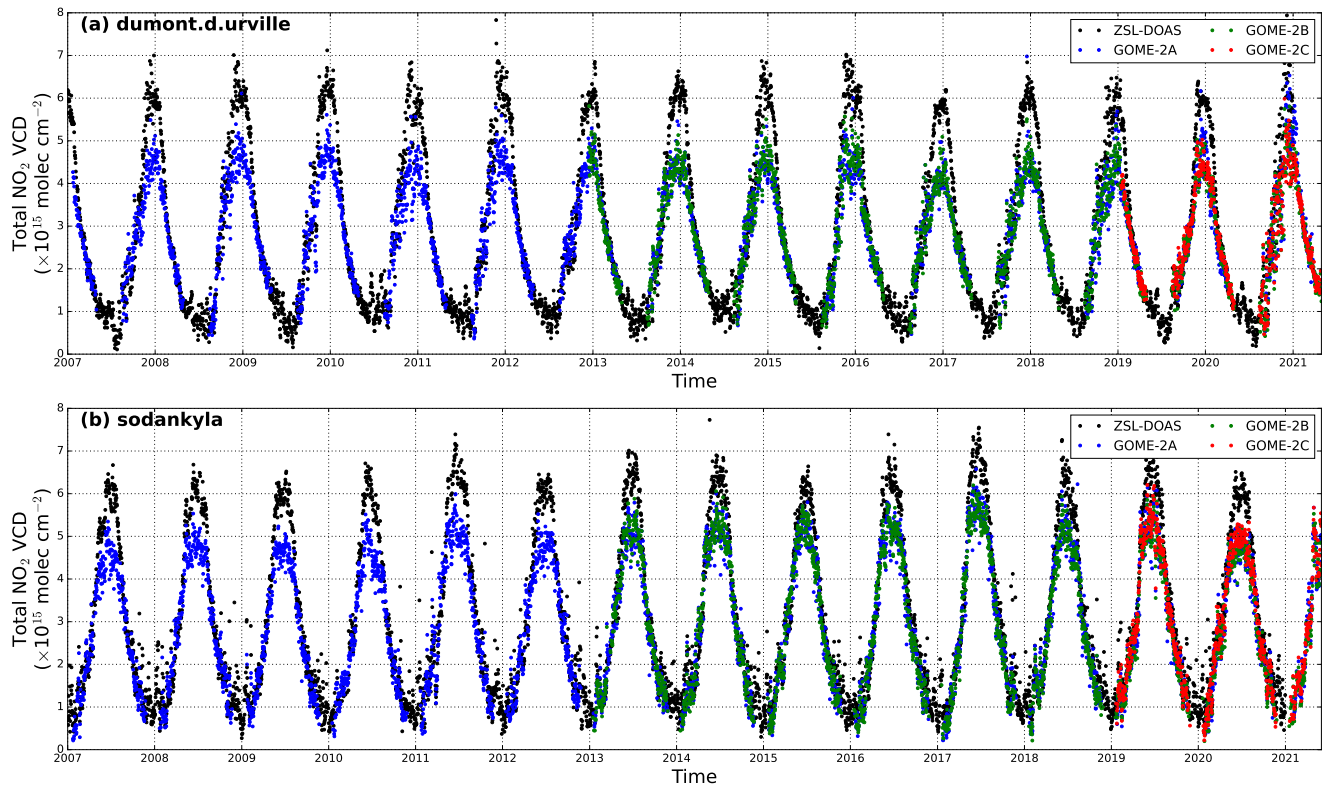
Figure 15. Time series of total column NO$_2$ measured by GOME-2A (blue), GOME-2B (green), GOME-2C (red) and ZSL-DOAS (black). Observations over (a) Dumont d'Urville, Antarctica and (b) Sodankylä, Finland are shown.
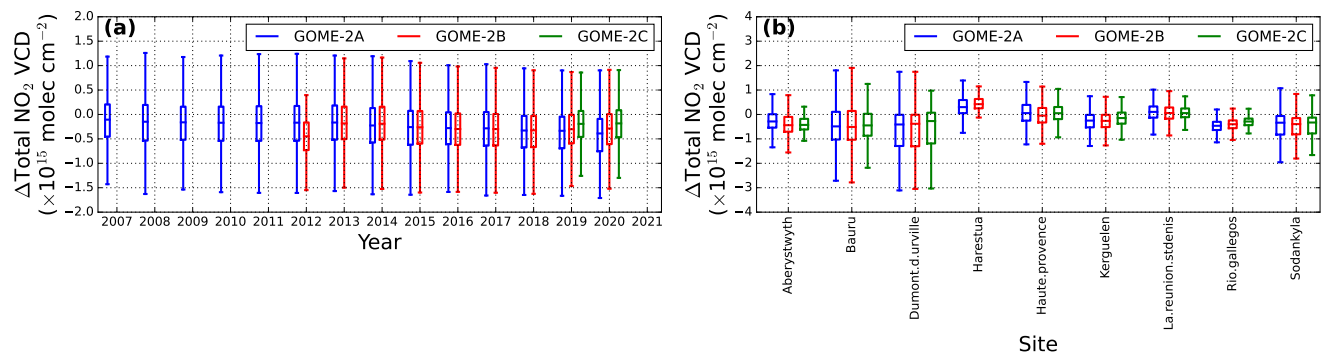
Figure 16. Comparison of total column NO$_2$ between ground-based ZSL-DOAS and GOME-2 observations. Data are sorted by year in (a), and measurement site in (b).

differences between GOME-2 and ZSL-DOAS observations are within 0.3×10^{15} molec cm^{-2} for most of the years and this bias does not show significant temporal variation. Box plots for each measurement site show significant negative bias for some sites, i.e., Dumont d'Urville and Sodankylä. The reason of the negative bias has been explained above.

5.2.3 Tropospheric column NO$_2$
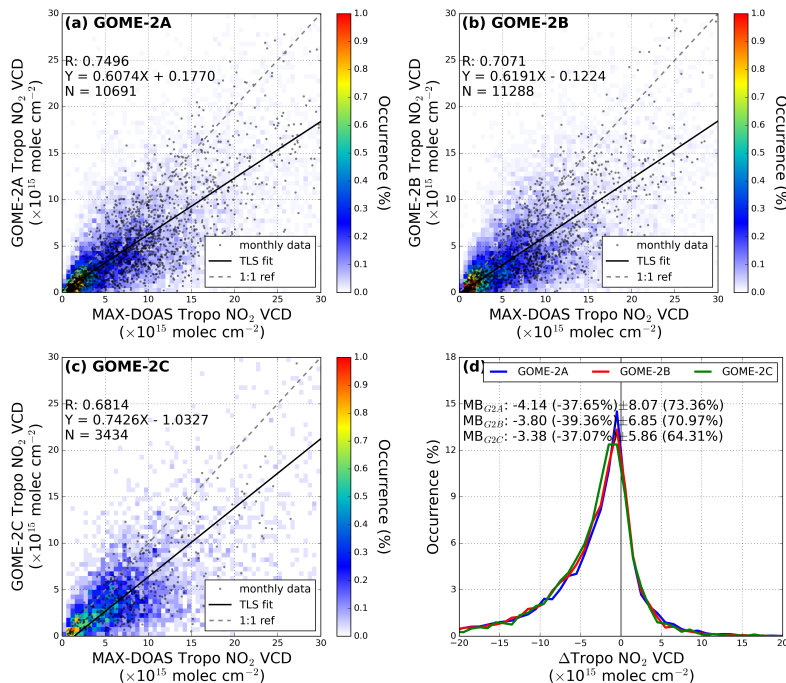
Figure 17. Comparison of daily and monthly tropospheric column NO$_2$ measured by the ground-based MAX-DOAS to (a) GOME-2A, (b) GOME-2B and (c) GOME-2C. Histograms of the difference of tropospheric column NO$_2$ between GOME-2 and MAX-DOAS are shown in (d). Co-located daily and monthly averaged data are used in the comparison. Total least squares regression is based on daily data.

Daily and monthly GOME-2 level 3 tropospheric column NO$_2$ are compared to the co-located MAX-DOAS observations. Figure 17 shows the density scatter plots for the comparison of tropospheric column NO$_2$ between GOME-2 and ground-based MAX-DOAS observations. Comparisons of GOME-2A, B and C data are shown in Figure 17a, b and c, respectively. Monthly data are also shown as black dots. Histograms of the differences between GOME-2 and MAX-DOAS observations are shown in Figure 17d. GOME-2 monthly tropospheric NO$_2$ data is consistent with the daily data, and daily data shows satisfactory correlation with ground-based MAX-DOAS observations with Pearson correlation coefficient (R) in a range of 0.68 to 0.75. However, GOME-2 tropospheric column NO$_2$ are in general $\sim$30 % lower than MAX-DOAS observations. The slopes of the total least squares fit for the comparisons of all three instruments vary from 0.61 to 0.74 with offset ranging from -1.03 to 0.18×10^{15} molec cm^{-2}. GOME-2 level 3 tropospheric NO$_2$ products on average show a negative bias of 3.38 -

4.14×10^{15} molec cm^{-2} (37 - 39 %). The underestimation is mainly related to the a-priori assign too low NO$_2$ concentration at the lower troposphere and spatial averaging effect over large satellite pixel. Previous study shows that using better a-priori vertical profile in GOME-2 retrieval reduces the underestimation of GOME-2 measurement by 15 - 20 % (Liu et al., 2019). The spatial averaging effect has also been estimated to result in an underestimation of 15 - 25 % in tropospheric column NO$_2$ over pollution hotspots (Chen et al., 2009; Ma et al., 2013; Chan et al., 2020b; Pinardi et al., 2020a). Considering that the sensitivity difference between satellite and ground-based MAX-DOAS measurements and the spatial averaging effect of large satellite footprint, the agreement between the two dataset is very satisfactory.
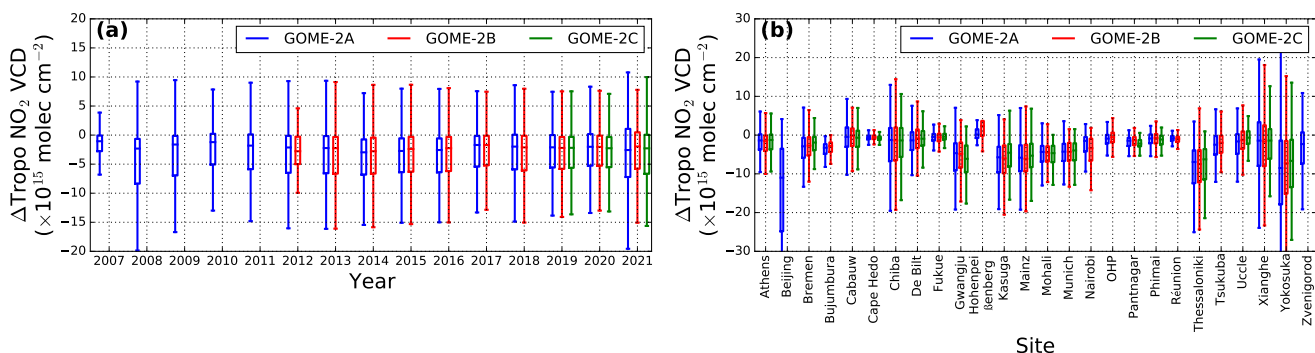
Figure 18. Comparison of tropospheric column NO$_2$ between ground-based MAX-DOAS and GOME-2 observations. Data are sorted by year in (a), and measurement site in (b).

Figure 18 shows box plots of the differences of tropospheric column NO$_2$ between GOME-2 level 3 product and co-located MAX-DOAS measurements. Data is sorted by the measurement year (Figure 18a) and measurement site (Figure 18b). The mean differences between GOME-2 and MAX-DOAS observations are $\sim 3 \times 10^{15}$ molec cm^{-2} for most of the years and this bias do not show significant temporal variation. Box plots for each measurement site show significant negative bias for some polluted sites, i.e., Beijing (China), Thessaloniki (Greece) and Yokosuka (Japan). The reason of the negative bias has been explained above. The underestimation is significantly reduced over rural areas, e.g., Cape Hedo (Japan), Cabauw (Netherlands) and Phimai (Thailand). These results are in line with the level 2 data that GOME-2 in general underestimates tropospheric column NO$_2$ over polluted areas.

5.2.4 Total column water vapour

Daily GOME-2 level 3 total column water vapour are compared to the co-located sun-photometer observations. Figure 19 shows the density scatter plots for the comparison of total column water vapour column between GOME-2 and ground-based sun-photometer observations. Comparisons of GOME-2A, B and C data are shown in Figure 14a, b and c, respectively. Histograms of the differences between GOME-2 and MAX-DOAS observations are shown in Figure 19d. Similar plots for monthly comparison are shown in Figure 20. GOME-2 monthly total column water vapour data is in general consistent with the daily
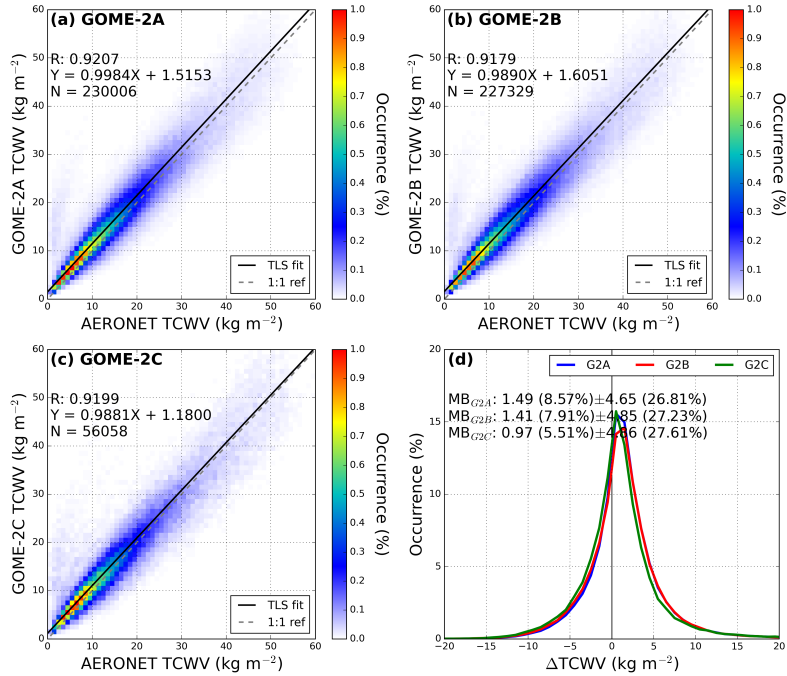
Figure 19. Comparison of daily total column water vapour measured by the sun photometer to (a) GOME-2A, (b) GOME-2B and (c) GOME-2C. Histograms of the difference between GOME-2 and sun-photometer are shown in (d). Co-located daily averaged data are used in the comparison.

data. GOME-2 daily observations are in good agreement with sun-photometer observations, with Pearson correlation coefficient (R) of $\sim$0.92 for all three instruments. Monthly comparison shows higher correlation coefficient (R) of $\sim$0.94. The slopes of least squares regression lines of daily comparison for all three GOME-2 sensors are very close to 1, while a small offset of $1.2 \text{-} 1.6 \, \mathrm{kg \, m^{-3}}$ is observed. Monthly comparison shows similar characteristic with the slope of regression close to 1

5   and offset of $1.1 \text{-} 1.6 \, \mathrm{kg \, m^{-3}}$. GOME-2 level 3 total column water vapour in general show a positive bias of $1.0 \text{-} 1.7 \, \mathrm{kg \, m^{-3}}$ ($6 \text{-} 9\,\%$). Considering that sun-photometer measurements are in general underestimating total column water vapour by $6\,\%$ (Pérez-Ramírez et al., 2014) the positive bias of $1.0 \text{-} 1.7 \, \mathrm{kg \, m^{-3}}$ is reasonable.

Figure 21 shows box plots of the statistic of the differences of total column water vapour between GOME-2 level 3 product and co-located sun-photometer measurements. Data is sorted by the measurement year (Figure 21a) and latitude band (Fig-

10   ure 21b). The bias between GOME-2 and sun-photometer observations is consistently at level of $1 \text{-} 2 \, \mathrm{kg \, m^{-3}}$ throughout the entire measurement period. The latitude dependency analysis shows larger variations in the tropics, while the variations are much smaller at higher latitudes. The absolute differences for measurements over Polar Regions are slightly higher. This is mainly due to multiple overpasses over Polar Regions during summer months and resulting temporal mismatch.
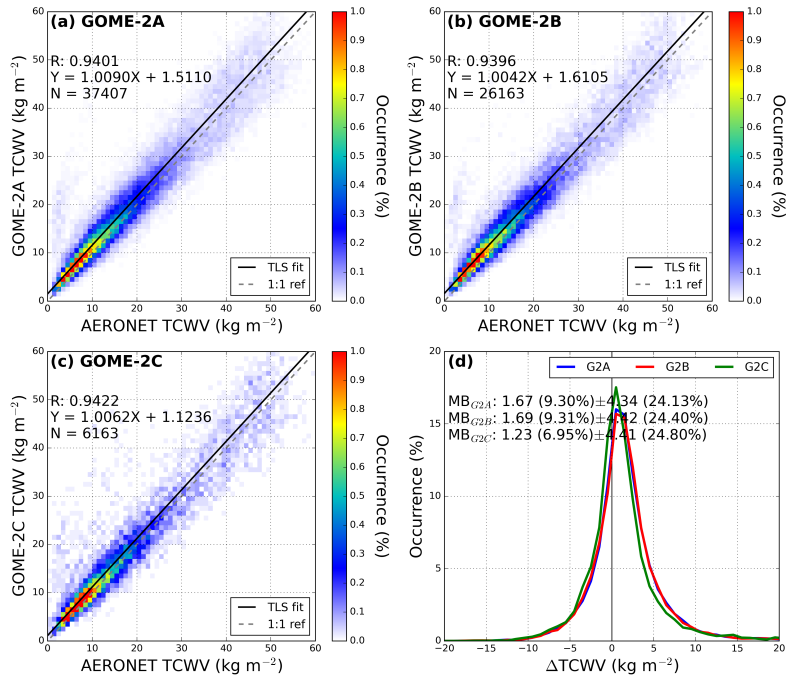
Figure 20. Comparison of monthly total column water vapour measured by the sun photometer to (a) GOME-2A, (b) GOME-2B and (c) GOME-2C. Histograms of the difference between GOME-2 and sun-photometer are shown in (d). Co-located monthly averaged data are used in the comparison.
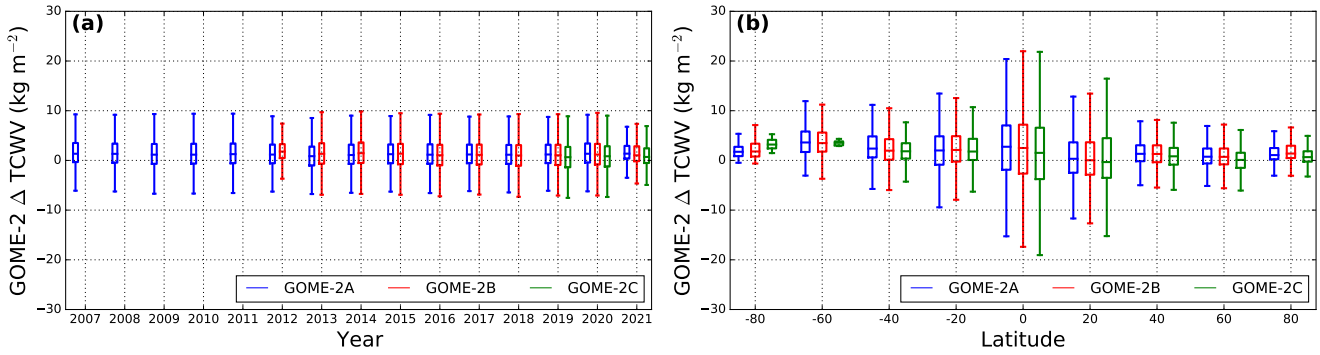
Figure 21. Comparison of TCWV between sun photometer and GOME-2 observations. Data are sorted by year in (a), and latitude in (b).
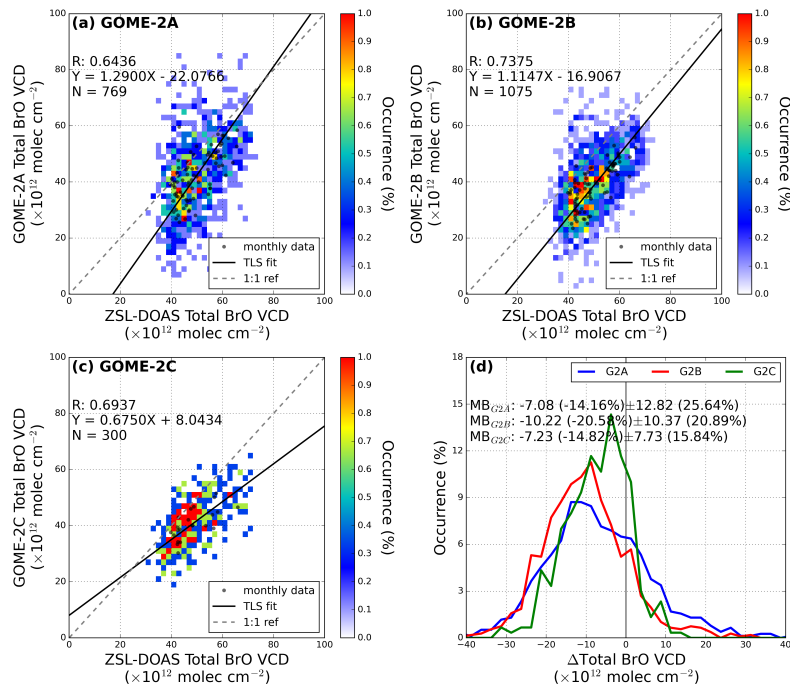
Figure 22. Comparison of daily and monthly total column BrO measured by the ground-based ZSL-DOAS at Harestua, Norway to (a) GOME-2A, (b) GOME-2B and (c) GOME-2C. Histograms of the difference of total column BrO between GOME-2 and MAX-DOAS observations are shown in (d). Co-located daily and monthly averaged data are used in the comparison. Total least squares regression is based on monthly data.

5.2.5 Total column BrO

Co-located daily and monthly GOME-2 level 3 total column BrO are compared to ZSL-DOAS observations at Harestua, Norway. Figure 22 shows the density scatter plots for the comparison of total column BrO between GOME-2 and ZSL-DOAS observations. Comparisons of GOME-2A, B and C data are shown in Figure 22a, b and c, respectively. Monthly data are also shown as black dots. Histograms of the differences between GOME-2 and ZSL-DOAS observations are shown in Figure 22d. We can see from the scatter plots that both GOME-2 and ZSL-DOAS BrO measurements are quite noisy, it is mainly due to the low absorption of BrO and thus low signal to noise ratio. Both daily and monthly GOME-2 level 3 data show quite good agreement with the ZSL-DOAS observations, with Pearson correlation coefficient (R) ranging from 0.64 to 0.74. In general, GOME-2 observations are underestimating BrO column by 7.0 - 10.2×10^{12} molec cm^{-2} (16 - 26 %). Please note that the comparison only covered one site in Norway and the numbers might vary in different part of the globe.

Figure 23 shows the time series of total column BrO measured at Harestua, Norway. Measurements from all three GOME-2 sensors show similar temporal variation trend with higher BrO level during winter/early spring and lower in summer which
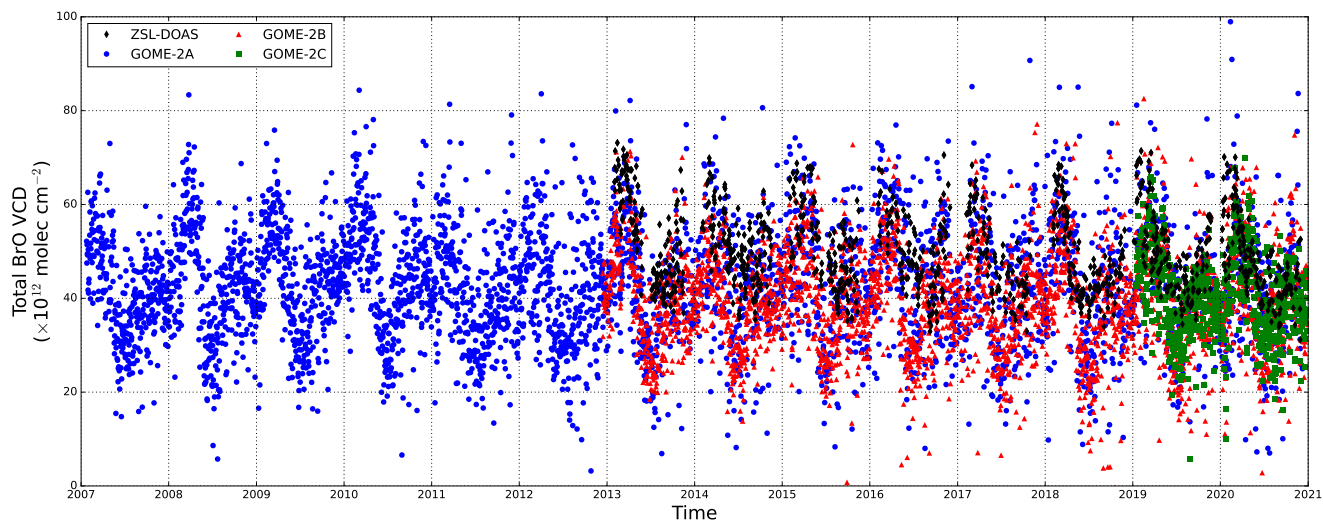
Figure 23. Time series of total column BrO measured by GOME-2A (blue), GOME-2B (green), GOME-2C (red) and ZSL-DOAS (black) at Harestua, Norway.

agrees with the ZSL-DOAS observations. However, GOME-2 observations are about $5\text{-}10 \times 10^{12}$ molec cm^{-2} lower than the ZSL-DOAS data. This underestimation has also been reported in the level 2 validation report (Theys et al., 2015a). Considering that the ZSL-DOAS data have been empirically corrected for the offset caused by instrumental effect, the agreement between GOME-2 and ZSL-DOAS is deemed very satisfactory.

5.2.6 Total column HCHO

Daily and monthly GOME-2 level 3 total column HCHO are compared to the co-located MAX-DOAS observations. Figure 24 shows the density scatter plots for the comparison of total column HCHO between GOME-2 and ground-based MAX-DOAS observations. Comparisons of GOME-2A, B and C data are shown in Figure 24a, b and c, respectively. Monthly data are also shown as black dots. Histograms of the differences between GOME-2 and MAX-DOAS observations are shown in Figure 24d. We can see from the scatter plots that both daily GOME-2 and MAX-DOAS HCHO measurements are quite noisy, it is mainly due to the low absorption of HCHO and thus low signal to noise ratio. However, when we look at the monthly averages, the GOME-2 level 3 data in general agrees with the ground-based MAX-DOAS observations. The Pearson correlation coefficient (R) between monthly GOME-2 and MAX-DOAS data ranges from 0.68 to 0.78. However, GOME-2 observations are in general underestimating total column HCHO by $20\text{-}25\,\%$. The slope of the total least squares regression line for the comparisons of all three instruments varies from 0.74 to 0.81 with offset ranging from -1.61 to -1.14×10^{15} molec cm^{-2}. GOME-2 level 3 total HCHO products on average show a small bias of -0.75 to 1.92×10^{15} molec cm^{-2} (-7 - 17 %) with standard deviation of 8.8 up to 11.4×10^{15} molec cm^{-2}. The underestimation is partly related to the a-prior profile used in GOME-2 retrieval and
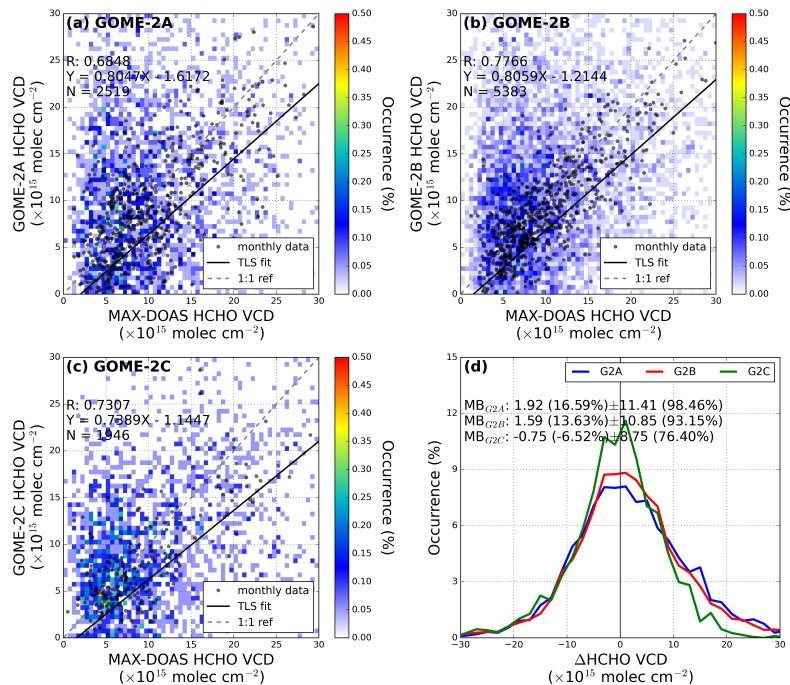
Figure 24. Comparison of daily and monthly total column HCHO measured by the ground-based MAX-DOAS to (a) GOME-2A, (b) GOME-2B and (c) GOME-2C. Histograms of the difference of total column HCHO between GOME-2 and MAX-DOAS are shown in (d). Co-located daily and monthly averaged data are used in the comparison. Total least squares regression is based on monthly data.

difference of sensitivity between satellite and ground-based observations. The underestimation of level 3 product is in line with the level 2 product. Previous studies show that the negative bias is significantly improved when the MAX-DOAS profiles are used for satellite column retrieval (De Smedt et al., 2015a, b). As the daily level 3 HCHO data is a bit noisy, it would be useful to further average the data spatially to reduce noise when looking into day to day variability or use the temporally averaged
5   product, i.e., the monthly product.

Figure 25 shows box plots of the statistic of the differences of total column HCHO between GOME-2 level 3 product and co-located MAX-DOAS measurements. Data is sorted by the measurement year (Figure 25a) and measurement site (Figure 25b). The mean differences between GOME-2 and MAX-DOAS observations are $1 - 2 \times 10^{15}$ molec cm^{-2} for most of the years and do not show significant temporal variation. Box plots for each measurement site show that GOME-2 significantly underesti-
10   mated HCHO column over polluted areas, i.e., Mexico City (Mexico) and Xianghe (China). The underestimation is related to the difference in sensitivity and this effect has been reported in previous level 2 validation studies for GOME-2 (De Smedt et al., 2015b; Pinardi et al., 2020b) as well as for other satellites (Chan et al., 2020b; De Smedt et al., 2021).
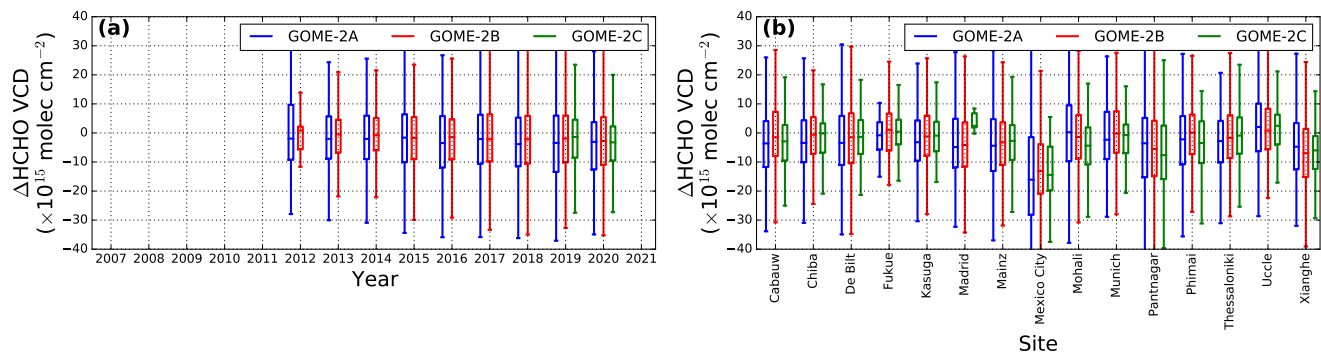
Figure 25. Comparison of total column HCHO between ground-based MAX-DOAS and GOME-2 observations. Data are sorted by year in (a), and measurement site in (b).
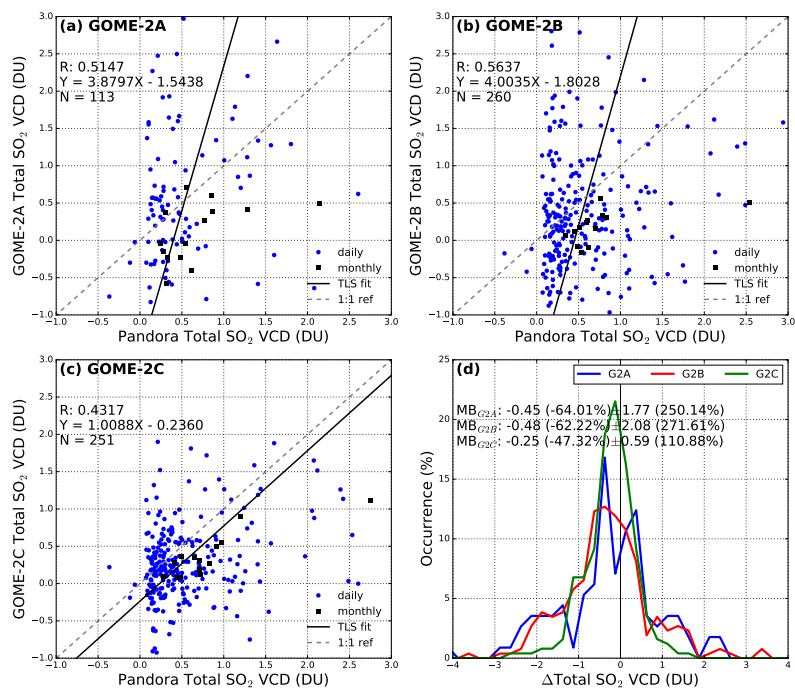
Figure 26. Comparison of daily and monthly total column SO_2 measured by Pandora instrument in Mexico City to (a) GOME-2A, (b) GOME-2B and (c) GOME-2C. Histograms of the difference of total column SO_2 between GOME-2 and Pandora observations are shown in (d). Co-located daily and monthly averaged data are used in the comparison. Total least squares regression is based on daily data.

5.2.7 Total column SO$_2$

The validation of volcanic SO$_2$ is very difficult due to the differences in volcanic plume injection height for each eruption. Therefore, it is often done in case study base, i.e., in previous validation reports (Theys et al., 2015b). In this study, we focus on the long term statistic and stability and therefore looking mainly into areas with significant SO$_2$ sources. Co-located daily and monthly GOME-2 level 3 total column SO$_2$ are compared to Pandora observations at Mexico City. Figure 26 shows the scatter plots for the comparison of total column SO$_2$ between GOME-2 and Pandora observations. Comparisons of GOME-2A, B and C data are shown in Figure 26a, b and c, respectively. Monthly data are also shown as black dots. Histograms of the differences between GOME-2 and Pandora observations are shown in Figure 26d. Due to the low absorption and abundancy of SO$_2$, both GOME-2 and Pandora measurements are quite noisy. Histogram shows that GOME-2 underestimated total column SO$_2$ by 0.25 to 0.48 DU (47 - 64 %). This underestimation is like related to the a priori profiles used in AMF calculations. The product assumes SO$_2$ plume at 6 km. If an a priori with SO$_2$ located in the lower troposphere is used in the AMF calculations, it would increase the retrieved SO$_2$ columns and reduces the underestimation. Please be aware that this is just a comparison over one site in Mexico and the numbers might vary over different part of the globe, especially due to the low concentration of SO$_2$ in general.
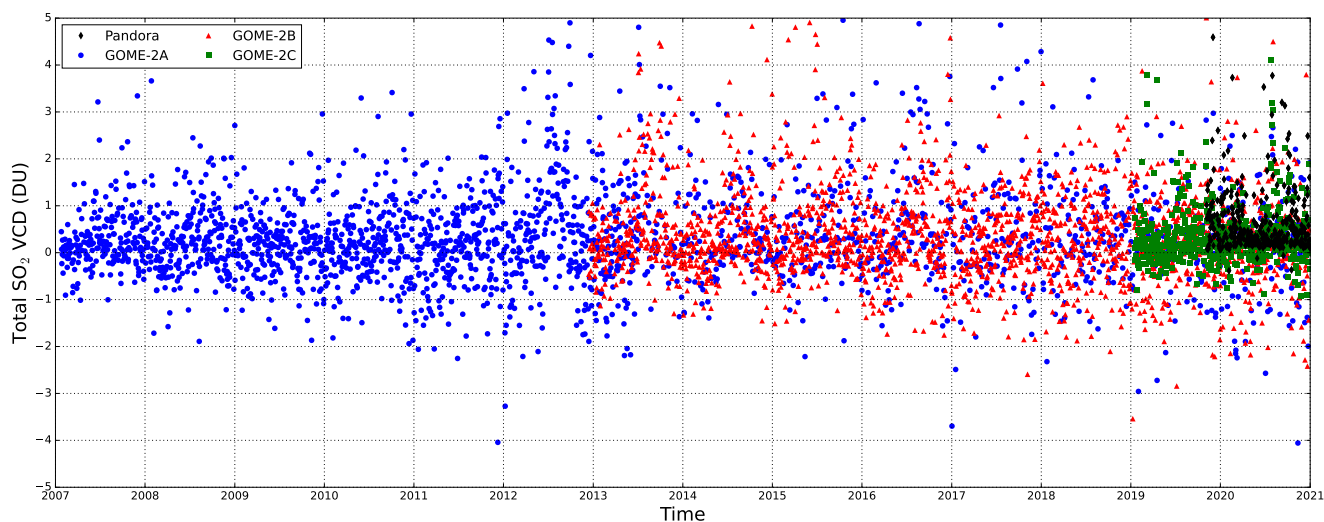
Figure 27. Time series of total column SO$_2$ measured by GOME-2A (blue), GOME-2B (green), GOME-2C (red) and Pandora (black) at Mexico City.

Figure 27 shows the time series of total column SO$_2$ measured at Mexico City. All three GOME-2 sensors show similar SO$_2$ columns. The overall averages are very close to zero and do not show any significant trend. Due to the low abundancy of SO$_2$ and low signal to noise ratio, there are considerable number of negative values. On the other hand, due to better signal to noise

ratio, only very few negative values measured by Pandora. Considering the measurement noise of GOME-2, the agreement between GOME-2 and Pandora datasets is reasonable.

6 Summary

We presented the new GOME-2 daily and monthly level 3 products which include total column O_3, total and tropospheric column NO_2, total column water vapour, total column BrO, total column HCHO and total column SO_2. Compared to satellite observations from OMI and TROPOMI which are measuring at noon/early afternoon, GOME-2 measurements in the morning provide addition information on the temporal/diurnal variation of these atmospheric trace gases. These additional information would be very useful for the studies of temporal/diurnal variations and photochemistry in the atmosphere. Details of the algorithm for level 2 to level 3 processing as well as the selection of appropriate spatial resolution for the level 3 products are shown. Verification and validation of each GOME-2 level 3 product are achieved by investigating the consistency among the three GOME-2 sensors and comparison to ground-based reference measurements.

The overlapping area weighting method is used for level 2 to level 3 processing. The spatial resolution of the GOME-2 level 3 products is selected based on sensitivity study. The consistency among three GOME-2 sensors is investigated through time series of global averages, zonal averages, and bias. Finally, the accuracy of the level 3 products is validated through the comparison to ground-based observations.

For the selection of appropriate spatial resolution of the GOME-2 level 3 data, we have re-sampled GOME-2 level 2 data onto various spatial resolutions, i.e., $0.1° \times 0.1°$, $0.25° \times 0.25°$ and $0.5° \times 0.5°$ and compared to the original level 2 data. All datasets show very similar spatial structures and the absolute values are consistency with the level 2 products. As expected, level 3 data sampled at higher spatial resolution (i.e., $0.1° \times 0.1°$) better preserved the original GOME-2 instrument footprint. However, lower resolution of $0.25° \times 0.25°$ also preserves the spatial pattern of fast varying tropospheric species, i.e., NO_2, reasonably well. While a rather strong smoothing/averaging effect is observed from data gridded with lower spatial resolution (i.e., $0.5° \times 0.5°$). Therefore, we concluded that the spatial resolution of $0.25° \times 0.25°$ is sufficient and appropriate for GOME-2 level 3 products.

The consistency of level 3 product among the three GOME-2 sensors are investigated. Global average time series plots show that total column ozone and water vapour products from all GOME-2 sensors are consistent, with only a small bias of up to 3 DU ($<1\%$) for ozone, and $0.9\,\mathrm{kg\,m^{-2}}$ ($<5\%$) for water vapour. For total and tropospheric column NO_2 products, GOME-2A and B measurements are consistent with each other, while GOME-2C data show significant discrepancy compared to the other two sensors. This is mainly due to the differences in processor versions (GDP 4.8 for GOME-2A & B and GDP 4.9 for GOME-2C) and spectral fitting band of NO_2. BrO observations from GOME-2B in general show a negative bias of $1.0\text{-}1.5 \times 10^{12}\,\mathrm{molec\,cm^{-2}}$ compared to GOME-2A and C. GOME-2A HCHO columns are $1.5\text{-}1.9 \times 10^{15}\,\mathrm{molec\,cm^{-2}}$ lower than GOME-2B and C measurements. This is due to the underestimation over Amazon, Southeast Asia, and Australia. Total column SO_2 observations from GOME-2C are on average 0.5 DU lower than GOME-2A and B, resulting a slightly negative global average. Slightly higher global average of SO_2 measured by GOME-2A and B is related to the high values taken under

extreme viewing geometry, i.e., high solar zenith angle. Please be reminded that BrO and SO_2 products are only validated against measurements at specific locations which might need to be further validated depending on the users applications.

For comparison of co-located GOME-2 level 3 data to ground-based observations, we found in general good agreement and the results are consistent with previous level 2 validation studies. We summarized the statistical result in Table 3.

Table 3. Summary of the GOME-2 level 3 data comparison to ground-based measurements.

GOME-2 Product	Reference Measurement	Correlation Coefficient (R)			Absolute Mean Bias			Relative Mean Bias (%)		
		GOME-2A	GOME-2B	GOME-2C	GOME-2A	GOME-2B	GOME-2C	GOME-2A	GOME-2B	GOME-2C
Total Column O_3[*]	Brewer	0.96	0.96	0.97	3.5 ± 14.7[a]	2.6 ± 14.5[a]	2.3 ± 13.9[a]	1.07 ± 4.48	0.81 ± 4.48	0.72 ± 4.30
Total Column NO_2[*]	ZSL-DOAS	0.85	0.86	0.89	-0.24 ± 0.65[b]	-0.29 ± 0.61[b]	-0.24 ± 0.55[b]	-8.36 ± 22.94	-10.31 ± 21.57	-8.58 ± 19.93
Tropospheric Column NO_2[*]	MAX-DOAS	0.75	0.71	0.68	-4.1 ± 8.1[b]	-3.8 ± 6.9[b]	-3.4 ± 5.9[b]	-37.65 ± 73.36	-39.36 ± 70.97	-37.07 ± 64.31
Total Column Water Vapour[*]	Sun-photometer	0.92	0.92	0.92	1.5 ± 4.7[c]	1.4 ± 4.9[c]	1.0 ± 4.9[c]	8.57 ± 26.81	7.91 ± 27.23	5.51 ± 27.61
Total Column BrO[#,+]	ZSL-DOAS	0.64	0.74	0.69	7.1 ± 12.8[d]	10.2 ± 10.4[d]	7.2 ± 7.7[d]	-14.16 ± 25.64	-20.58 ± 20.89	-14.82 ± 15.84
Total Column HCHO[#]	MAX-DOAS	0.68	0.78	0.73	1.9 ± 11.4[b]	1.6 ± 10.9[b]	-0.8 ± 8.8[b]	16.59 ± 98.46	13.63 ± 93.15	-6.52 ± 76.40
Total Column SO_2[*,+]	Pandora	0.51	0.56	0.43	0.45 ± 1.8[a]	0.48 ± 2.1[a]	2.5 ± 0.6[a]	-64.01 ± 250.14	-62.22 ± 271.61	-47.32 ± 110.88

[a] unit in DU, [b] unit in 10^{15} molec cm^{-2}, [c] unit in kg m^{-2}, [d] unit in 10^{12} molec cm^{-2}

[*] regression is computed based on daily data, [#] regression is computed based on monthly data

[+] based on comparison at a single location

All biases are calculated based on daily data

From the results above, we conclude that the daily and monthly GOME-2 level 3 products of total column O_3, total and tropospheric column NO_2, total column water vapour, total column BrO, total column HCHO and total column SO_2 for GOME-2A, GOME-2B and GOME-2C are consistent and fulfil the product requirements.

7 Data availability

The GOME-2 level 3 products described in this paper are available to public via EUMETSAT's Satellite Application Facility on Atmospheric Composition Monitoring (https://acsaf.org). DOIs: daily products 10.15770/EUM_SAF_AC_0048; monthly products 10.15770/EUM_SAF_AC_0049

Author contributions. KLC conceptualized the paper, devised the methodology, developed the algorithm and validated the data sets. KLC and PV managed the project. KLC, KPH, RL, PH and DL provided supports on GOME-2 level 2 data. KLC, GP, MVR, FH, TW, VK, AB, AP, HI, YK, HT, YC, KP, JC, AC, UF, AR, JM, NB, RH, CRC and MW provided ground-based reference data. KLC prepared the manuscript with contributions from all the co-authors.

Competing interests. The authors declare that they have no conflict of interest.

Acknowledgements. The work described in this paper was carried out within the framework of the European Organization for the Exploitation of Meteorological Satellites (EUMETSAT) Satellite Application Facility on Atmospheric Composition Monitoring (AC SAF) Continuous Development and Operations Phase (CDOP-3) and Associated Scientist Project. We acknowledge EUMETSAT and AC SAF for the pro-

duction of the GOME-2 level 2 and 3 data. We thank WOUDC, NDACC, NIDFORVAL and AERONET in harmonizing and managing the ground-based data sets used in this study. Work by Hitoshi Irie on ground-based MAX-DOAS observations data was supported the Environment Research and Technology Development Fund (JPMEERF20215005) of the Environmental Restoration and Conservation Agency of Japan, JSPS KAKENHI (grant numbers JP20H04320, JP21K12227, JP22H03727, and JP22H05004), the JAXA 3rd research announcement on the Earth Observations (grant number 19RT000351), and the Virtual Laboratory (VL) project by the Ministry of Education, Culture, Sports, Science and Technology (MEXT), Japan. The scientific results and conclusions, as well as any views or opinions expressed herein, are those of the author and do not necessarily reflect those of NOAA, the Department of Commerce or other data providers.

References

Alexandrov, M. D., Schmid, B., Turner, D. D., Cairns, B., Oinas, V., Lacis, A. A., Gutman, S. I., Westwater, E. R., Smirnov, A., and Eilers, J.: Columnar water vapor retrievals from multifilter rotating shadowband radiometer data, Journal of Geophysical Research: Atmospheres, 114, https://doi.org/10.1029/2008JD010543, 2009.

Anderson, G. P., Clough, S. A., Kneizys, F., Chetwynd, J. H., and Shettle, E. P.: AFGL atmospheric constituent profiles (0.120 km), Tech. rep., AIR FORCE GEOPHYSICS LAB HANSCOM AFB MA, 1986.

Antón, M., Loyola, D., López, M., Vilaplana, J. M., Bañón, M., Zimmer, W., and Serrano, A.: Comparison of GOME-2/MetOp total ozone data with Brewer spectroradiometer data over the Iberian Peninsula, Annales Geophysicae, 27, 1377–1386, https://doi.org/10.5194/angeo-27-1377-2009, 2009.

Balis, D., Kroon, M., Koukouli, M. E., Brinksma, E. J., Labow, G., Veefkind, J. P., and McPeters, R. D.: Validation of Ozone Monitoring Instrument total ozone column measurements using Brewer and Dobson spectrophotometer ground-based observations, Journal of Geophysical Research: Atmospheres, 112, https://doi.org/10.1029/2007JD008796, 2007a.

Balis, D., Lambert, J.-C., Van Roozendael, M., Spurr, R., Loyola, D., Livschitz, Y., Valks, P., Amiridis, V., Gerard, P., Granville, J., and Zehner, C.: Ten years of GOME/ERS2 total ozone data – The new GOME data processor (GDP) version 4: 2. Ground-based validation and comparisons with TOMS V7/V8, Journal of Geophysical Research: Atmospheres, 112, https://doi.org/10.1029/2005JD006376, 2007b.

Bennouna, Y. S., Torres, B., Cachorro, V. E., Ortiz de Galisteo, J. P., and Toledano, C.: The evaluation of the integrated water vapour annual cycle over the Iberian Peninsula from EOS-MODIS against different ground-based techniques, Quarterly Journal of the Royal Meteorological Society, 139, 1935–1956, https://doi.org/10.1002/qj.2080, 2013.

Bovensmann, H., Burrows, J. P., Buchwitz, M., Frerick, J., Noël, S., Rozanov, V. V., Chance, K. V., and Goede, A. P. H.: SCIA-MACHY: Mission Objectives and Measurement Modes, Journal of the Atmospheric Sciences, 56, 127 – 150, https://doi.org/10.1175/1520-0469(1999)056<0127:SMOAMM>2.0.CO;2, 1999.

Brinksma, E. J., Pinardi, G., Volten, H., Braak, R., Richter, A., Schönhardt, A., van Roozendael, M., Fayt, C., Hermans, C., Dirksen, R. J., Vlemmix, T., Berkhout, A. J. C., Swart, D. P. J., Oetjen, H., Wittrock, F., Wagner, T., Ibrahim, O. W., de Leeuw, G., Moerman, M., Curier, R. L., Celarier, E. A., Cede, A., Knap, W. H., Veefkind, J. P., Eskes, H. J., Allaart, M., Rothe, R., Piters, A. J. M., and Levelt, P. F.: The 2005 and 2006 DANDELIONS NO₂ and aerosol intercomparison campaigns, Journal of Geophysical Research: Atmospheres, 113, https://doi.org/10.1029/2007JD008808, 2008.

Bruns, M., Bovensmann, H., Richter, A., and Burrows, J. P.: A Stratospheric BrO Climatology for the GOME-2 instruments, Tech. rep., 2003.

Burrows, J. P., Weber, M., Buchwitz, M., Rozanov, V., Ladstätter-Weißenmayer, A., Richter, A., DeBeek, R., Hoogen, R., Bramstedt, K., Eichmann, K.-U., et al.: The global ozone monitoring experiment (GOME): Mission concept and first scientific results, Journal of the Atmospheric Sciences, 56, 151–175, https://doi.org/10.1175/1520-0469(1999)056<0151:TGOMEG>2.0.CO;2, 1999.

Callies, J., Corpaccioli, E., Eisinger, M., Hahne, A., and Lefebvre, A.: GOME-2-Metop's second-generation sensor for operational ozone monitoring, ESA bulletin, 102, 28–36, 2000.

Celarier, E. A., Brinksma, E. J., Gleason, J. F., Veefkind, J. P., Cede, A., Herman, J. R., Ionov, D., Goutail, F., Pommereau, J.-P., Lambert, J.-C., van Roozendael, M., Pinardi, G., Wittrock, F., Schönhardt, A., Richter, A., Ibrahim, O. W., Wagner, T., Bojkov, B., Mount, G., Spinei, E., Chen, C. M., Pongetti, T. J., Sander, S. P., Bucsela, E. J., Wenig, M. O., Swart, D. P. J., Volten, H., Kroon, M., and Lev-

elt, P. F.: Validation of Ozone Monitoring Instrument nitrogen dioxide columns, Journal of Geophysical Research: Atmospheres, 113, https://doi.org/10.1029/2007JD008908, 2008.

Chan, K. L., Pöhler, D., Kuhlmann, G., Hartl, A., Platt, U., and Wenig, M. O.: NO_2 measurements in Hong Kong using LED based long path differential optical absorption spectroscopy, Atmospheric Measurement Techniques, 5, 901–912, https://doi.org/10.5194/amt-5-901-2012, 2012.

Chan, K. L., Hartl, A., Lam, Y. F., Xie, P. H., Liu, W. Q., Cheung, H. M., Lampel, J., Pöhler, D., Li, A., Xu, J., Zhou, H. J., Ning, Z., and Wenig, M.: Observations of tropospheric NO_2 using ground based MAX-DOAS and OMI measurements during the Shanghai World Expo 2010, Atmospheric Environment, 119, 45–58, https://doi.org/10.1016/j.atmosenv.2015.08.041, 2015.

Chan, K. L., Wiegner, M., Wenig, M., and Pöhler, D.: Observations of tropospheric aerosols and NO_2 in Hong Kong over 5 years using ground based MAX-DOAS, Science of The Total Environment, 619-620, 1545 – 1556, https://doi.org/10.1016/j.scitotenv.2017.10.153, 2018.

Chan, K. L., Wang, Z., Ding, A., Heue, K.-P., Shen, Y., Wang, J., Zhang, F., Shi, Y., Hao, N., and Wenig, M.: MAX-DOAS measurements of tropospheric NO_2 and HCHO in Nanjing and a comparison to ozone monitoring instrument observations, Atmospheric Chemistry and Physics, 19, 10 051–10 071, https://doi.org/10.5194/acp-19-10051-2019, 2019.

Chan, K. L., Valks, P., Slijkhuis, S., Köhler, C., and Loyola, D.: Total column water vapor retrieval for Global Ozone Monitoring Experience-2 (GOME-2) visible blue observations, Atmospheric Measurement Techniques, 13, 4169–4193, https://doi.org/10.5194/amt-13-4169-2020, 2020a.

Chan, K. L., Wiegner, M., van Geffen, J., De Smedt, I., Alberti, C., Cheng, Z., Ye, S., and Wenig, M.: MAX-DOAS measurements of tropospheric NO_2 and HCHO in Munich and the comparison to OMI and TROPOMI satellite observations, Atmospheric Measurement Techniques, 13, 4499–4520, https://doi.org/10.5194/amt-13-4499-2020, 2020b.

Chen, D., Zhou, B., Beirle, S., Chen, L. M., and Wagner, T.: Tropospheric NO_2 column densities deduced from zenith-sky DOAS measurements in Shanghai, China, and their application to satellite validation, Atmospheric Chemistry and Physics, 9, 3641–3662, https://doi.org/10.5194/acp-9-3641-2009, 2009.

Chipperfield, M. P.: Multiannual simulations with a three-dimensional chemical transport model, Journal of Geophysical Research: Atmospheres, 104, 1781–1805, https://doi.org/10.1029/98JD02597, 1999.

Clough, S. A. and Iacono, M. J.: Line-by-line calculation of atmospheric fluxes and cooling rates: 2. Application to carbon dioxide, ozone, methane, nitrous oxide and the halocarbons, Journal of Geophysical Research: Atmospheres, 100, 16 519–16 535, https://doi.org/10.1029/95JD01386, 1995.

Compernolle, S., Verhoelst, T., Pinardi, G., Granville, J., Hubert, D., Keppens, A., Niemeijer, S., Rino, B., Bais, A., Beirle, S., Boersma, F., Burrows, J. P., De Smedt, I., Eskes, H., Goutail, F., Hendrick, F., Lorente, A., Pazmino, A., Piters, A., Peters, E., Pommereau, J.-P., Remmers, J., Richter, A., van Geffen, J., Van Roozendael, M., Wagner, T., and Lambert, J.-C.: Validation of Aura-OMI QA4ECV NO_2 climate data records with ground-based DOAS networks: the role of measurement and comparison uncertainties, Atmospheric Chemistry and Physics, 20, 8017–8045, https://doi.org/10.5194/acp-20-8017-2020, 2020.

De Smedt, I., Van Roozendael, M., Stavrakou, T., Müller, J.-F., Lerot, C., Theys, N., Valks, P., Hao, N., and van der A, R.: Improved retrieval of global tropospheric formaldehyde columns from GOME-2/MetOp-A addressing noise reduction and instrumental degradation issues, Atmospheric Measurement Techniques, 5, 2933–2949, https://doi.org/10.5194/amt-5-2933-2012, 2012.

De Smedt, I., Pinardi, G., Yu, H., Hendrick, F., Gielen, C., Hao, N., Begoin, M., and Valks, P.: O3M SAF Validation Report for GOME-2A & B Total HCHO, https://acsaf.org/docs/vr/Validation_Report_NTO_OTO_DR_HCHO_GDP48_Oct_2015.pdf, 2015a.

De Smedt, I., Stavrakou, T., Hendrick, F., Danckaert, T., Vlemmix, T., Pinardi, G., Theys, N., Lerot, C., Gielen, C., Vigouroux, C., Hermans, C., Fayt, C., Veefkind, P., Müller, J.-F., and Van Roozendael, M.: Diurnal, seasonal and long-term variations of global formaldehyde columns inferred from combined OMI and GOME-2 observations, Atmospheric Chemistry and Physics, 15, 12 519–12 545, https://doi.org/10.5194/acp-15-12519-2015, 2015b.

5   De Smedt, I., Pinardi, G., Vigouroux, C., Compernolle, S., Bais, A., Benavent, N., Boersma, F., Chan, K.-L., Donner, S., Eichmann, K.-U., Hedelt, P., Hendrick, F., Irie, H., Kumar, V., Lambert, J.-C., Langerock, B., Lerot, C., Liu, C., Loyola, D., Piters, A., Richter, A., Rivera Cárdenas, C., Romahn, F., Ryan, R. G., Sinha, V., Theys, N., Vlietinck, J., Wagner, T., Wang, T., Yu, H., and Van Roozendael, M.: Comparative assessment of TROPOMI and OMI formaldehyde observations and validation against MAX-DOAS network column measurements, Atmospheric Chemistry and Physics, 21, 12 561–12 593, https://doi.org/10.5194/acp-21-12561-2021, 2021.

10 Diedrich, H., Preusker, R., Lindstrot, R., and Fischer, J.: Retrieval of daytime total columnar water vapour from MODIS measurements over land surfaces, Atmospheric Measurement Techniques, 8, 823–836, https://doi.org/10.5194/amt-8-823-2015, 2015.

Drosoglou, T., Bais, A. F., Zyrichidou, I., Kouremeti, N., Poupkou, A., Liora, N., Giannaros, C., Koukouli, M. E., Balis, D., and Melas, D.: Comparisons of ground-based tropospheric NO_2 MAX-DOAS measurements to satellite observations with the aid of an air quality model over the Thessaloniki area, Greece, Atmospheric Chemistry and Physics, 17, 5829–5849, https://doi.org/10.5194/acp-17-5829-2017, 2017.

15 Eleftheratos, K., Isaksen, I., Zerefos, C., Nastos, P., Tourpali, K., and Rognerud, B.: Ozone Variations Derived by a Chemical Transport Model, Water, Air, & Soil Pollution, 224, 1585, https://doi.org/10.1007/s11270-013-1585-2, 2013.

Fried, A., Cantrell, C., Olson, J., Crawford, J. H., Weibring, P., Walega, J., Richter, D., Junkermann, W., Volkamer, R., Sinreich, R., Heikes, B. G., O'Sullivan, D., Blake, D. R., Blake, N., Meinardi, S., Apel, E., Weinheimer, A., Knapp, D., Perring, A., Cohen, R. C., Fuelberg, H., Shetter, R. E., Hall, S. R., Ullmann, K., Brune, W. H., Mao, J., Ren, X., Huey, L. G., Singh, H. B., Hair, J. W., Riemer, D., Diskin,

20 G., and Sachse, G.: Detailed comparisons of airborne formaldehyde measurements with box models during the 2006 INTEX-B and MILAGRO campaigns: potential evidence for significant impacts of unmeasured and multi-generation volatile organic carbon compounds, Atmospheric Chemistry and Physics, 11, 11 867–11 894, https://doi.org/10.5194/acp-11-11867-2011, 2011.

Garane, K., Lerot, C., Coldewey-Egbers, M., Verhoelst, T., Koukouli, M. E., Zyrichidou, I., Balis, D. S., Danckaert, T., Goutail, F., Granville, J., Hubert, D., Keppens, A., Lambert, J.-C., Loyola, D., Pommereau, J.-P., Van Roozendael, M., and Zehner, C.: Quality assessment of

25 the Ozone_cci Climate Research Data Package (release 2017) – Part 1: Ground-based validation of total ozone column data products, Atmospheric Measurement Techniques, 11, 1385–1402, https://doi.org/10.5194/amt-11-1385-2018, 2018.

Garane, K., Koukouli, M.-E., Verhoelst, T., Lerot, C., Heue, K.-P., Fioletov, V., Balis, D., Bais, A., Bazureau, A., Dehn, A., Goutail, F., Granville, J., Griffin, D., Hubert, D., Keppens, A., Lambert, J.-C., Loyola, D., McLinden, C., Pazmino, A., Pommereau, J.-P., Redondas, A., Romahn, F., Valks, P., Van Roozendael, M., Xu, J., Zehner, C., Zerefos, C., and Zimmer, W.: TROPOMI/S5P total ozone column data:

30 global ground-based validation and consistency with other satellite missions, Atmospheric Measurement Techniques, 12, 5263–5287, https://doi.org/10.5194/amt-12-5263-2019, 2019.

Garane, K., Chan, K. L., Koukouli, M.-E., Loyola, D., and Balis, D.: TROPOMI/S5P Total Column Water Vapor Validation against AERONET ground-based measurements, Atmospheric Measurement Techniques Discussions, 2022, 1–22, https://doi.org/10.5194/amt-2022-94, 2022.

35 Grossi, M., Valks, P., Loyola, D., Aberle, B., Slijkhuis, S., Wagner, T., Beirle, S., and Lang, R.: Total column water vapour measurements from GOME-2 MetOp-A and MetOp-B, Atmospheric Measurement Techniques, 8, 1111–1133, https://doi.org/10.5194/amt-8-1111-2015, 2015.

Grzegorski, M.: Cloud retrieval from UV/VIS satellite instruments:(SCIAMACHY and GOME), Ph.D. thesis, University of Heidelberg, 2009.

Hao, N., Koukouli, M. E., Inness, A., Valks, P., Loyola, D. G., Zimmer, W., Balis, D. S., Zyrichidou, I., Van Roozendael, M., Lerot, C., and Spurr, R. J. D.: GOME-2 total ozone columns from MetOp-A/MetOp-B and assimilation in the MACC system, Atmospheric Measurement Techniques, 7, 2937–2951, https://doi.org/10.5194/amt-7-2937-2014, 2014.

Hebestreit, K., Stutz, J., Rosen, D., Matveiv, V., Peleg, M., Luria, M., and Platt, U.: DOAS Measurements of Tropospheric Bromine Oxide in Mid-Latitudes, Science, 283, 55–57, https://doi.org/10.1126/science.283.5398.55, 1999.

Hegglin, M. I., Fahey, D. W., McFarland, M., Montzka, S. A., Nash, E. R., et al.: Twenty Questions and Answers About the Ozone Layer: 2014 Update-Scientific Assessment of Ozone Depletion: 2014, 2015.

Hendrick, F., Van Roozendael, M., Chipperfield, M. P., Dorf, M., Goutail, F., Yang, X., Fayt, C., Hermans, C., Pfeilsticker, K., Pommereau, J.-P., Pyle, J. A., Theys, N., and De Mazière, M.: Retrieval of stratospheric and tropospheric BrO profiles and columns using ground-based zenith-sky DOAS observations at Harestua, 60 °N, Atmospheric Chemistry and Physics, 7, 4869–4885, https://doi.org/10.5194/acp-7-4869-2007, 2007.

Holben, B., Eck, T., Slutsker, I., Tanre, D., Buis, J., Setzer, A., Vermote, E., Reagan, J., Kaufman, Y., Nakajima, T., Lavenu, F., Jankowiak, I., and Smirnov, A.: AERONET - A Federated Instrument Network and Data Archive for Aerosol Characterization, Remote Sensing of Environment, 66, 1–16, https://doi.org/10.1016/S0034-4257(98)00031-5, 1998.

Holben, B. N., Tanre, D., Smirnov, A., Eck, T. F., Slutsker, I., Abuhassan, N., Newcomb, W. W., Schafer, J. S., Chatenet, B., Lavenu, F., Kaufman, Y. J., Castle, J. V., Setzer, A., Markham, B., Clark, D., Frouin, R., Halthore, R., Karneli, A., O'Neill, N. T., Pietras, C., Pinker, R. T., Voss, K., and Zibordi, G.: An emerging ground-based aerosol climatology: Aerosol optical depth from AERONET, Journal of Geophysical Research: Atmospheres, 106, 12 067–12 097, https://doi.org/10.1029/2001JD900014, 2001.

Hörmann, C., Sihler, H., Bobrowski, N., Beirle, S., Penning de Vries, M., Platt, U., and Wagner, T.: Systematic investigation of bromine monoxide in volcanic plumes from space by using the GOME-2 instrument, Atmospheric Chemistry and Physics, 13, 4749–4781, https://doi.org/10.5194/acp-13-4749-2013, 2013.

Hörmann, C., Sihler, H., Beirle, S., Penning de Vries, M., Platt, U., and Wagner, T.: Seasonal variation of tropospheric bromine monoxide over the Rann of Kutch salt marsh seen from space, Atmospheric Chemistry and Physics, 16, 13 015–13 034, https://doi.org/10.5194/acp-16-13015-2016, 2016.

Ionov, D. V., Timofeyev, Y. M., Sinyakov, V. P., Semenov, V. K., Goutail, F., Pommereau, J.-P., Bucsela, E. J., Celarier, E. A., and Kroon, M.: Ground-based validation of EOS-Aura OMI NO_2 vertical column data in the midlatitude mountain ranges of Tien Shan (Kyrgyzstan) and Alps (France), Journal of Geophysical Research: Atmospheres, 113, https://doi.org/10.1029/2007JD008659, 2008.

Irie, H., Kanaya, Y., Akimoto, H., Tanimoto, H., Wang, Z., Gleason, J. F., and Bucsela, E. J.: Validation of OMI tropospheric NO_2 column data using MAX-DOAS measurements deep inside the North China Plain in June 2006: Mount Tai Experiment 2006, Atmospheric Chemistry and Physics, 8, 6577–6586, https://doi.org/10.5194/acp-8-6577-2008, 2008.

Irie, H., Kanaya, Y., Takashima, H., Gleason, J. F., and Wang, Z.: Characterization of OMI Tropospheric NO_2 Measurements in East Asia Based on a Robust Validation Comparison, Scientific Online Letters on the Atmosphere, 5, 117–120, https://doi.org/10.2151/sola.2009-030, 2009.

Irie, H., Boersma, K. F., Kanaya, Y., Takashima, H., Pan, X., and Wang, Z. F.: Quantitative bias estimates for tropospheric NO_2 columns retrieved from SCIAMACHY, OMI, and GOME-2 using a common standard for East Asia, Atmospheric Measurement Techniques, 5, 2403–2411, https://doi.org/10.5194/amt-5-2403-2012, 2012.

Irie, H., Muto, T., Itahashi, S., Kurokawa, J., and Uno, I.: Turnaround of Tropospheric Nitrogen Dioxide Pollution Trends in China, Japan, and South Korea, Scientific Online Letters on the Atmosphere, 12, 170–174, https://doi.org/10.2151/sola.2016-035, 2016.

Kanaya, Y., Irie, H., Takashima, H., Iwabuchi, H., Akimoto, H., Sudo, K., Gu, M., Chong, J., Kim, Y. J., Lee, H., Li, A., Si, F., Xu, J., Xie, P.-H., Liu, W.-Q., Dzhola, A., Postylyakov, O., Ivanov, V., Grechko, E., Terpugova, S., and Panchenko, M.: Long-term MAX-DOAS network observations of NO_2 in Russia and Asia (MADRAS) during the period 2007–2012: instrumentation, elucidation of climatology, and comparisons with OMI satellite observations and global model simulations, Atmospheric Chemistry and Physics, 14, 7909–7927, https://doi.org/10.5194/acp-14-7909-2014, 2014.

Kerr, J. B., Asbridge, I. A., and Evans, W. F. J.: Intercomparison of total ozone measured by the Brewer and Dobson spectrophotometers at Toronto, Journal of Geophysical Research: Atmospheres, 93, 11 129–11 140, https://doi.org/10.1029/JD093iD09p11129, 1988.

Khokhar, M., Frankenberg, C., Van Roozendael, M., Beirle, S., Kühl, S., Richter, A., Platt, U., and Wagner, T.: Satellite observations of atmospheric SO_2 from volcanic eruptions during the time-period of 1996–2002, Advances in Space Research, 36, 879–887, https://doi.org/10.1016/j.asr.2005.04.114, atmospheric Remote Sensing: Earth's Surface, Troposphere, Stratosphere and Mesosphere- I, 2005.

Kiehl, J. T. and Trenberth, K. E.: Earth's Annual Global Mean Energy Budget, Bulletin of the American Meteorological Society, 78, 197 – 208, https://doi.org/10.1175/1520-0477(1997)078<0197:EAGMEB>2.0.CO;2, 1997.

Klaes, K. D., Cohen, M., Buhler, Y., Schlüssel, P., Munro, R., Luntama, J.-P., von Engeln, A., Clérigh, E. Ó., Bonekamp, H., Ackermann, J., et al.: An introduction to the EUMETSAT polar system, Bulletin of the American Meteorological Society, 88, 1085–1096, https://doi.org/10.1175/BAMS-88-7-1085, 2007.

Koelemeijer, R. B. A., de Haan, J. F., and Stammes, P.: A database of spectral surface reflectivity in the range 335–772 nm derived from 5.5 years of GOME observations, Journal of Geophysical Research: Atmospheres, 108, https://doi.org/10.1029/2002JD002429, 2003.

Koukouli, M. E., Balis, D. S., Loyola, D., Valks, P., Zimmer, W., Hao, N., Lambert, J.-C., Van Roozendael, M., Lerot, C., and Spurr, R. J. D.: Geophysical validation and long-term consistency between GOME-2/MetOp-A total ozone column and measurements from the sensors GOME/ERS-2, SCIAMACHY/ENVISAT and OMI/Aura, Atmospheric Measurement Techniques, 5, 2169–2181, https://doi.org/10.5194/amt-5-2169-2012, 2012.

Koukouli, M. E., Lerot, C., Granville, J., Goutail, F., Lambert, J.-C., Pommereau, J.-P., Balis, D., Zyrichidou, I., Van Roozendael, M., Coldewey-Egbers, M., Loyola, D., Labow, G., Frith, S., Spurr, R., and Zehner, C.: Evaluating a new homogeneous total ozone climate data record from GOME/ERS-2, SCIAMACHY/Envisat, and GOME-2/MetOp-A, Journal of Geophysical Research: Atmospheres, 120, 12,296–12,312, https://doi.org/10.1002/2015JD023699, 2015.

Kuhlmann, G., Hartl, A., Cheung, H. M., Lam, Y. F., and Wenig, M. O.: A novel gridding algorithm to create regional trace gas maps from satellite observations, Atmospheric Measurement Techniques, 7, 451–467, https://doi.org/10.5194/amt-7-451-2014, 2014.

Kumar, V., Beirle, S., Dörner, S., Mishra, A. K., Donner, S., Wang, Y., Sinha, V., and Wagner, T.: Long-term MAX-DOAS measurements of NO_2, HCHO, and aerosols and evaluation of corresponding satellite data products over Mohali in the Indo-Gangetic Plain, Atmospheric Chemistry and Physics, 20, 14 183–14 235, https://doi.org/10.5194/acp-20-14183-2020, 2020.

Lang, R., Casadio, S., Maurellis, A. N., and Lawrence, M. G.: Evaluation of the GOME Water Vapor Climatology 1995–2002, Journal of Geophysical Research: Atmospheres, 112, https://doi.org/10.1029/2006JD008246, 2007.

Levelt, P., Van den Oord, G. H. J., Dobber, M., Malkki, A., Visser, H., de Vries, J., Stammes, P., Lundell, J., and Saari, H.: The ozone monitoring instrument, Geoscience and Remote Sensing, IEEE Transactions on, 44, 1093–1101, https://doi.org/10.1109/TGRS.2006.872333, 2006.

Li, X., Brauers, T., Hofzumahaus, A., Lu, K., Li, Y. P., Shao, M., Wagner, T., and Wahner, A.: MAX-DOAS measurements of NO_2, HCHO and CHOCHO at a rural site in Southern China, Atmospheric Chemistry and Physics, 13, 2133–2151, https://doi.org/10.5194/acp-13-2133-2013, 2013.

Liu, S., Valks, P., Pinardi, G., De Smedt, I., Yu, H., Beirle, S., and Richter, A.: An improved total and tropospheric NO_2 column retrieval for GOME-2, Atmospheric Measurement Techniques, 12, 1029–1057, https://doi.org/10.5194/amt-12-1029-2019, 2019.

Liu, S., Valks, P., Pinardi, G., Xu, J., Argyrouli, A., Lutz, R., Tilstra, L. G., Huijnen, V., Hendrick, F., and Van Roozendael, M.: An improved air mass factor calculation for nitrogen dioxide measurements from the Global Ozone Monitoring Experiment-2 (GOME-2), Atmospheric Measurement Techniques, 13, 755–787, https://doi.org/10.5194/amt-13-755-2020, 2020.

Loyola, D. G., Thomas, W., Livschitz, Y., Ruppert, T., Albert, P., and Hollmann, R.: Cloud Properties Derived From GOME/ERS-2 Backscatter Data for Trace Gas Retrieval, IEEE Transactions on Geoscience and Remote Sensing, 45, 2747–2758, https://doi.org/10.1109/TGRS.2007.901043, 2007.

Loyola, D. G., Koukouli, M. E., Valks, P., Balis, D. S., Hao, N., Van Roozendael, M., Spurr, R. J. D., Zimmer, W., Kiemle, S., Lerot, C., and Lambert, J.-C.: The GOME-2 total column ozone product: Retrieval algorithm and ground-based validation, Journal of Geophysical Research: Atmospheres, 116, https://doi.org/10.1029/2010JD014675, 2011.

Loyola, D. G., Gimeno García, S., Lutz, R., Argyrouli, A., Romann, F., Spurr, R. J. D., Pedergnana, M., Doicu, A., Molina García, V., and Schüssler, O.: The operational cloud retrieval algorithms from TROPOMI on board Sentinel-5 Precursor, Atmospheric Measurement Techniques, 11, 409–427, https://doi.org/10.5194/amt-11-409-2018, 2018.

Lutz, R., Loyola, D., Gimeno García, S., and Romahn, F.: OCRA radiometric cloud fractions for GOME-2 on MetOp-A/B, Atmospheric Measurement Techniques, 9, 2357–2379, https://doi.org/10.5194/amt-9-2357-2016, 2016.

Ma, J. Z., Beirle, S., Jin, J. L., Shaiganfar, R., Yan, P., and Wagner, T.: Tropospheric NO_2 vertical column densities over Beijing: results of the first three years of ground-based MAX-DOAS measurements (2008–2011) and satellite validation, Atmospheric Chemistry and Physics, 13, 1547–1567, https://doi.org/10.5194/acp-13-1547-2013, 2013.

Martins, V. S., Lyapustin, A., Wang, Y., Giles, D. M., Smirnov, A., Slutsker, I., and Korkin, S.: Global validation of columnar water vapor derived from EOS MODIS-MAIAC algorithm against the ground-based AERONET observations, Atmospheric Research, 225, 181–192, https://doi.org/10.1016/j.atmosres.2019.04.005, 2019.

Merlaud, A., Theys, N., Hendrick, F., van Gent, J., Pinardi, G., Van Roozendael, M., Chan, K. L., Heue, K. P., and Valks, P.: Validation report of GOME-2 GDP 4.9 BrO column data for MetOp-C Operational Readiness Review, Tech. rep., EUMETSAT AC SAF, https://acsaf.org/docs/vr/Validation_Report_OTO_BrO_May_2020.pdf, 2020.

Müller, J.-F. and Stavrakou, T.: Inversion of CO and NO_x emissions using the adjoint of the IMAGES model, Atmospheric Chemistry and Physics, 5, 1157–1186, https://doi.org/10.5194/acp-5-1157-2005, 2005.

Munro, R., Lang, R., Klaes, D., Poli, G., Retscher, C., Lindstrot, R., Huckle, R., Lacan, A., Grzegorski, M., Holdak, A., Kokhanovsky, A., Livschitz, J., and Eisinger, M.: The GOME-2 instrument on the Metop series of satellites: instrument design, calibration, and level 1 data processing - an overview, Atmospheric Measurement Techniques, 9, 1279–1301, https://doi.org/10.5194/amt-9-1279-2016, 2016.

Noël, S., Mieruch, S., Bovensmann, H., and Burrows, J. P.: Preliminary results of GOME-2 water vapour retrievals and first applications in polar regions, Atmospheric Chemistry and Physics, 8, 1519–1529, https://doi.org/10.5194/acp-8-1519-2008, 2008.

Palmer, P. I., Jacob, D. J., Chance, K., Martin, R. V., Spurr, R. J. D., Kurosu, T. P., Bey, I., Yantosca, R., Fiore, A., and Li, Q.: Air mass factor formulation for spectroscopic measurements from satellites: Application to formaldehyde retrievals from the Global Ozone Monitoring Experiment, Journal of Geophysical Research: Atmospheres, 106, 14 539–14 550, https://doi.org/10.1029/2000JD900772, 2001.

Pérez-Ramírez, D., Whiteman, D. N., Smirnov, A., Lyamani, H., Holben, B. N., Pinker, R., Andrade, M., and Alados-Arboledas, L.: Evaluation of AERONET precipitable water vapor versus microwave radiometry, GPS, and radiosondes at ARM sites, Journal of Geophysical Research: Atmospheres, 119, 9596–9613, https://doi.org/10.1002/2014JD021730, 2014.

Pinardi, G., Yu, H., Lambert, J.-C., Granville, J., van Gent, J., Van Roozendael, M., and Valks, P.: Validation report of GOME-2 GDP 4.9 NO$_2$ column data for MetOp-C Operational Readiness Review, Tech. rep., EUMETSAT AC SAF, https://acsaf.org/docs/vr/Validation_Report_NTO_OTO_NO2_Nov_2019.pdf, 2019.

Pinardi, G., Van Roozendael, M., Hendrick, F., Theys, N., Abuhassan, N., Bais, A., Boersma, F., Cede, A., Chong, J., Donner, S., Drosoglou, T., Dzhola, A., Eskes, H., Frieß, U., Granville, J., Herman, J. R., Holla, R., Hovila, J., Irie, H., Kanaya, Y., Karagkiozidis, D., Kouremeti, N., Lambert, J.-C., Ma, J., Peters, E., Piters, A., Postylyakov, O., Richter, A., Remmers, J., Takashima, H., Tiefengraber, M., Valks, P., Vlemmix, T., Wagner, T., and Wittrock, F.: Validation of tropospheric NO$_2$ column measurements of GOME-2A and OMI using MAX-DOAS and direct sun network observations, Atmospheric Measurement Techniques, 13, 6141–6174, https://doi.org/10.5194/amt-13-6141-2020, 2020a.

Pinardi, G., Yu, H., Van Roozendael, M., Van Gent, J., Chan, K. L., and Valks, P.: O3M SAF Validation Report for GOME-2C Total HCHO, https://acsaf.org/docs/vr/Validation_Report_NTO_OTO_HCHO_May_2020.pdf, 2020b.

Platt, U. and Stutz, J.: Differential optical absorption spectroscopy - principles and applications, Springer, 2008.

Platt, U. and Wagner, T.: Satellite mapping of enhanced BrO concentrations in the troposphere, Nature, 395, 486–490, https://doi.org/10.1038/26723, 1998.

Richter, A., Wittrock, F., Eisinger, M., and Burrows, J. P.: GOME observations of tropospheric BrO in northern hemispheric spring and summer 1997, Geophysical Research Letters, 25, 2683–2686, https://doi.org/10.1029/98GL52016, 1998.

Richter, A., Wittrock, F., Ladstätter-Weißenmayer, A., and Burrows, J.: GOME measurements of stratospheric and tropospheric BrO, Advances in Space Research, 29, 1667–1672, https://doi.org/10.1016/S0273-1177(02)00123-0, 2002.

Rix, M., Valks, P., Hao, N., van Geffen, J., Clerbaux, C., Clarisse, L., Coheur, P.-F., Loyola R., D. G., Erbertseder, T., Zimmer, W., and Emmadi, S.: Satellite Monitoring of Volcanic Sulfur Dioxide Emissions for Early Warning of Volcanic Hazards, IEEE Journal of Selected Topics in Applied Earth Observations and Remote Sensing, 2, 196–206, https://doi.org/10.1109/JSTARS.2009.2031120, 2009.

Rix, M., Valks, P., Hao, N., Loyola, D., Schlager, H., Huntrieser, H., Flemming, J., Koehler, U., Schumann, U., and Inness, A.: Volcanic SO$_2$, BrO and plume height estimations using GOME-2 satellite measurements during the eruption of Eyjafjallajökull in May 2010, Journal of Geophysical Research: Atmospheres, 117, https://doi.org/10.1029/2011JD016718, 2012.

Shindell, D. T., Faluvegi, G., Koch, D. M., Schmidt, G. A., Unger, N., and Bauer, S. E.: Improved Attribution of Climate Forcing to Emissions, Science, 326, 716–718, https://doi.org/10.1126/science.1174760, 2009.

Solomon, S., Schmeltekopf, A. L., and Sanders, R. W.: On the interpretation of zenith sky absorption measurements, Journal of Geophysical Research: Atmospheres, 92, 8311–8319, https://doi.org/10.1029/JD092iD07p08311, 1987.

Spurr, R.: LIDORT and VLIDORT: Linearized pseudo-spherical scalar and vector discrete ordinate radiative transfer models for use in remote sensing retrieval problems, pp. 229–275, Springer Berlin Heidelberg, Berlin, Heidelberg, https://doi.org/10.1007/978-3-540-48546-9_7, 2008.

Spurr, R. J.: VLIDORT: A linearized pseudo-spherical vector discrete ordinate radiative transfer code for forward model and retrieval studies in multilayer multiple scattering media, Journal of Quantitative Spectroscopy and Radiative Transfer, 102, 316–342, https://doi.org/10.1016/j.jqsrt.2006.05.005, 2006.

Theys, N., Van Roozendael, M., Dils, B., Hendrick, F., Hao, N., and De Mazière, M.: First satellite detection of volcanic bromine monoxide emission after the Kasatochi eruption, Geophysical Research Letters, 36, https://doi.org/10.1029/2008GL036552, 2009.

Theys, N., Van Roozendael, M., Hendrick, F., Yang, X., De Smedt, I., Richter, A., Begoin, M., Errera, Q., Johnston, P. V., Kreher, K., and De Mazière, M.: Global observations of tropospheric BrO columns using GOME-2 satellite data, Atmospheric Chemistry and Physics, 11, 1791–1811, https://doi.org/10.5194/acp-11-1791-2011, 2011.

Theys, N., Hendrick, F., Van Gent, J., Van Roozendael, M., Hao, N., and Valks, P.: O3M SAF Validation Report for GOME-2A & B Total BrO, https://acsaf.org/docs/vr/Validation_Report_OTO_DR_BrO_GDP48_Dec_2015.pdf, 2015a.

Theys, N., Koukouli, M., Pinardi, G., Van Roozendael, M., Balis, D., Hedelt, H., and Valks, P.: O3M SAF Validation Report for GOME-2A & B SO$_2$ vertical columns, https://acsaf.org/docs/vr/Validation_Report_NTO_OTO_DR_SO2_GDP48_Dec_2015.pdf, 2015b.

Valks, P., Pinardi, G., Richter, A., Lambert, J.-C., Hao, N., Loyola, D., Van Roozendael, M., and Emmadi, S.: Operational total and tropospheric NO$_2$ column retrieval for GOME-2, Atmospheric Measurement Techniques, 4, 1491–1514, https://doi.org/10.5194/amt-4-1491-2011, 2011.

Valks, P., Chan, K. L., Hedelt, P., Slijkhuis, S., , and Lutz, R.: Algorithm Theoretical Basis Document for GOME-2 Total Column Products of Ozone, NO2, BrO, SO2, H2O, HCHO, OClO and Cloud Properties (GDP 4.8/4.9), Tech. rep., EUMETSAT AC SAF, https://acsaf.org/docs/atbd/Algorithm_Theoretical_Basis_Document_NTO_OTO_Nov_2019.pdf, 2019.

Van Roozendael, M., Loyola, D., Spurr, R., Balis, D., Lambert, J.-C., Livschitz, Y., Valks, P., Ruppert, T., Kenter, P., Fayt, C., and Zehner, C.: Ten years of GOME/ERS-2 total ozone data—The new GOME data processor (GDP) version 4: 1. Algorithm description, Journal of Geophysical Research: Atmospheres, 111, https://doi.org/10.1029/2005JD006375, 2006.

Vandaele, A. C., Hermans, C., Fally, S., Carleer, M., Colin, R., Merienne, M.-F., Jenouvrier, A., and Coquart, B.: High-resolution Fourier transform measurement of the NO$_2$ visible and near-infrared absorption cross sections: Temperature and pressure effects, Journal of Geophysical Research: Atmospheres, 107, ACH 3–1–ACH 3–12, https://doi.org/10.1029/2001JD000971, 2002.

Veefkind, J., Aben, I., McMullan, K., Förster, H., de Vries, J., Otter, G., Claas, J., Eskes, H., de Haan, J., Kleipool, Q., van Weele, M., Hasekamp, O., Hoogeveen, R., Landgraf, J., Snel, R., Tol, P., Ingmann, P., Voors, R., Kruizinga, B., Vink, R., Visser, H., and Levelt, P.: TROPOMI on the ESA Sentinel-5 Precursor: A GMES mission for global observations of the atmospheric composition for climate, air quality and ozone layer applications, Remote Sensing of Environment, 120, 70 – 83, https://doi.org/10.1016/j.rse.2011.09.027, 2012.

Verhoelst, T., Compernolle, S., Pinardi, G., Lambert, J.-C., Eskes, H. J., Eichmann, K.-U., Fjæraa, A. M., Granville, J., Niemeijer, S., Cede, A., Tiefengraber, M., Hendrick, F., Pazmiño, A., Bais, A., Bazureau, A., Boersma, K. F., Bognar, K., Dehn, A., Donner, S., Elokhov, A., Gebetsberger, M., Goutail, F., Grutter de la Mora, M., Gruzdev, A., Gratsea, M., Hansen, G. H., Irie, H., Jepsen, N., Kanaya, Y., Karagkiozidis, D., Kivi, R., Kreher, K., Levelt, P. F., Liu, C., Müller, M., Navarro Comas, M., Piters, A. J. M., Pommereau, J.-P., Portafaix, T., Prados-Roman, C., Puentedura, O., Querel, R., Remmers, J., Richter, A., Rimmer, J., Rivera Cárdenas, C., Saavedra de Miguel, L., Sinyakov, V. P., Stremme, W., Strong, K., Van Roozendael, M., Veefkind, J. P., Wagner, T., Wittrock, F., Yela González, M., and Zehner, C.: Ground-based validation of the Copernicus Sentinel-5P TROPOMI NO$_2$ measurements with the NDACC ZSL-DOAS, MAX-DOAS and Pandonia global networks, Atmospheric Measurement Techniques, 14, 481–510, https://doi.org/10.5194/amt-14-481-2021, 2021.

Vigouroux, C., Hendrick, F., Stavrakou, T., Dils, B., De Smedt, I., Hermans, C., Merlaud, A., Scolas, F., Senten, C., Vanhaelewyn, G., Fally, S., Carleer, M., Metzger, J.-M., Müller, J.-F., Van Roozendael, M., and De Mazière, M.: Ground-based FTIR and MAX-DOAS observations of formaldehyde at Réunion Island and comparisons with satellite and model data, Atmospheric Chemistry and Physics, 9, 9523–9544, https://doi.org/10.5194/acp-9-9523-2009, 2009.

Wagner, T., Heland, J., Zöger, M., and Platt, U.: A fast H_2O total column density product from GOME - Validation with in-situ aircraft measurements, Atmospheric Chemistry and Physics, 3, 651–663, https://doi.org/10.5194/acp-3-651-2003, 2003.

Wagner, T., Beirle, S., Grzegorski, M., and Platt, U.: Global trends (1996-2003) of total column precipitable water observed by Global Ozone Monitoring Experiment (GOME) on ERS-2 and their relation to near-surface temperature, Journal of Geophysical Research: Atmospheres, 111, https://doi.org/10.1029/2005JD006523, 2006.

Wagner, T., Beirle, S., Deutschmann, T., Grzegorski, M., and Platt, U.: Satellite monitoring of different vegetation types by differential optical absorption spectroscopy (DOAS) in the red spectral range, Atmospheric Chemistry and Physics, 7, 69–79, https://doi.org/10.5194/acp-7-69-2007, 2007.

Wang, Y., Beirle, S., Lampel, J., Koukouli, M., De Smedt, I., Theys, N., Li, A., Wu, D., Xie, P., Liu, C., Van Roozendael, M., Stavrakou, T., Müller, J.-F., and Wagner, T.: Validation of OMI, GOME-2A and GOME-2B tropospheric NO_2, SO_2 and HCHO products using MAX-DOAS observations from 2011 to 2014 in Wuxi, China: investigation of the effects of priori profiles and aerosols on the satellite products, Atmospheric Chemistry and Physics, 17, 5007–5033, https://doi.org/10.5194/acp-17-5007-2017, 2017.

Wenig, M., Kühl, S., Beirle, S., Bucsela, E., Jähne, B., Platt, U., Gleason, J., and Wagner, T.: Retrieval and analysis of stratospheric NO_2 from the Global Ozone Monitoring Experiment, Journal of Geophysical Research: Atmospheres, 109, https://doi.org/10.1029/2003JD003652, 2004.

Wenig, M. O., Cede, A. M., Bucsela, E. J., Celarier, E. A., Boersma, K. F., Veefkind, J. P., Brinksma, E. J., Gleason, J. F., and Herman, J. R.: Validation of OMI tropospheric NO_2 column densities using direct-Sun mode Brewer measurements at NASA Goddard Space Flight Center, Journal of Geophysical Research: Atmospheres, 113, https://doi.org/10.1029/2007JD008988, 2008.

Wennberg, P. O., Cohen, R. C., Stimpfle, R. M., Koplow, J. P., Anderson, J. G., Salawitch, R. J., Fahey, D. W., Woodbridge, E. L., Keim, E. R., Gao, R. S., Webster, C. R., May, R. D., Toohey, D. W., Avallone, L. M., Proffitt, M. H., Loewenstein, M., Podolske, J. R., Chan, K. R., and Wofsy, S. C.: Removal of Stratospheric O_3 by Radicals: In Situ Measurements of OH, HO_2, NO, NO_2, ClO, and BrO, Science, 266, 398–404, https://doi.org/10.1126/science.266.5184.398, 1994.